Science News

How PCBs May Alter In Utero, Neonatal Brain Development

ScienceDaily (Apr. 14, 2009) — In three new studies — including one appearing online today in the Public Library of Science - Biology (PLoS - Biology) — UC Davis researchers provide compelling evidence of how low levels of polychlorinated biphenyls (PCBs) alter the way brain cells develop.

The findings could explain at last — some 30 years after the toxic chemicals were banned in the United States — the associations between exposure of the developing nervous system to PCBs and behavioral deficits in children.

"We've never really understood the mechanism by which PCBs produce neurobehavioral problems in children," said Isaac N. Pessah, professor of molecular biosciences, director of the UC Davis Center for Children's Environmental Health and co-author of all three studies.

"With these studies we have now shown — from the whole animal level to the molecular level — how PCBs alter the development and excitability of brain cells. And that could explain why PCBs are associated with higher rates of neurodevelopmental and behavioral disorders," said Pessah, who is also a researcher with the UC Davis M.I.N.D. Institute.

Together, the studies — published within one month of each other — make a compelling case for the mechanism behind PCBs' harmful effects on human neurological development.

In a groundbreaking animal study appearing online in late March in *Environmental Health Perspectives*, Pessah and his colleagues found that low-level, in utero and neonatal exposure to PCBs altered the development of brain cells in rats.

A second study in *Toxicology and Applied Pharmacology*, also appearing online in March, showed which PCBs affected brain-cell circuits in the hippocampus, a region of the brain known to be impaired in several complex neurodevelopmental disorders including autism.

The third study, which appears online April 13 in *PLoS - Biology*, describes in detail the molecular target of the PCBs, the calcium channels known as ryanodine receptors, and shows that PCBs lock these calcium channels in the open position, which likely contributes to the over-excitations on neural circuits observed in the two other studies.

PCBs were used in a wide variety of products including transformers and capacitors and other electronic components, pesticides and flame retardants, from the early to late 20th century. Their production was banned in the 1970s due to the high toxicity of most PCBs. They do not break down in the environment and accumulate in animals' bodies. Exposure occurs when chemicals dumped into the environment years ago are released into the air or leach into groundwater and contaminate fish that people eat.

"Not only will this help us deal with current exposures," Pessah said, "but we can also identify similar compounds that have come on line since PCBs were banned and make better decisions about which ones we restrict and which new ones we allow to come to market."

PCBs have been implicated in epidemiological studies as an environmental cause of diverse neurodevelopmental disorders,

See Also:

Health & Medicine
- Nervous System
- Brain Tumor

Mind & Brain
- Child Development
- Intelligence

Earth & Climate
- Sustainability
- Environmental Issues

Reference
- PCB
- Dioxin
- Sensory neuron
- Fetal alcohol spectrum disorder

Related Stories

Women Exposed To High Levels of Pollutant PCB More Likely To Give Birth To Female Children (July 16, 2008) — Women exposed to high levels of PCBs (polychlorinated biphenyls -- a group of banned environmental pollutants) are less likely to give birth to male children. A new study found that among women from ... > *read more*

Bacterium Could Treat PCBs Without The Need For Dredging (Mar. 13, 2007) — Researchers have discovered a tiny bacterium that could one day transform the way we remove polychlorinated biphenyls (PCBs) from our environment. The organism could be the key to developing methods ... > *read more*

Some Wood Floor Finishes Are A Likely Source Of PCB Exposure (Jan. 17, 2008) — Old wood floor finishes in some homes may be an overlooked source of exposure to the now banned environmental pollutants polychlorinated biphenyls (PCBs). PCBs are persistent organic pollutants ... > *read more*

PCBs May Threaten Killer Whale Populations For 30-60 Years (Sep. 10, 2007) — Orcas or killer whales may continue to suffer the effects of contamination with polychlorinated biphenyls (PCBs) for the next 30 to 60 years, despite 1970s-era regulations that have reduced overall ... > *read more*

Fetal Exposure To PCBs Impacts Reproductive Markers Of Children And Grandchildren Of Exposed Animals (May 27, 2008) — Since the 1962 publication of Silent Spring by Rachel Carson, awareness of how environmental toxicants can impact fertility has increased. Researchers now provide evidence that adverse reproductive ... > *read more*

PCBs Found in Soon-to-Be-Dredged Indiana Harbor and Ship Canal (Jan. 12, 2010) — Researchers have confirmed that sediments of the Indiana Harbor and Ship Canal (IHSC) in East Chicago, Ind., are contaminated with polychlorinated biphenyls (PCBs). The IHSC, part of

Just In:
'Un-Growth Hormone' Increases Longevity

Science Video News

Baby Thinking
Radiologists have developed a new device to understand brain activity. It is a collection of fiber optic cables attached to a flexible cap placed. ... > *full story*

Kinesiologists Design Tiny Treadmill To Help Balance Baby Steps In Down Syndrome Infants

MRIs Peek into the Brains of Synesthesia Patients

Pediatric Neurologists Use MRI to Understand How Strokes Impair Verbal Abilities

more science videos

Breaking News

... from NewsDaily.com

Gene study shows Neanderthals had eastern cousins

Placebos help, even when patients know about them

Brazil to step up crackdown on "biopiracy" in 2011

Africa has two species of elephants, not one

Invasive species lie in wait, strike after decades

more science news

In Other News ...

North Korea may have new atom test to boost heir: South

Toyota settles suit over California crash for $10 million

U.S. defends permits for deals in sanctioned nations

Rahm Emanuel gets green light to run for Chicago mayor

Russian Duma could

said, "and we hope to identify those and help get them off the market."

In addition to Lein and Pessah, authors of the Environmental Health Perspectives study include Dongren Yang (co-first author) of Oregon Health & Science University, Kyung Ho Kim (co-first author) and Andrew Phimister of UC Davis, Adam Bachstetter and Ronald Mervis of the University of South Florida, Thomas Ward and Prasada Kodavanti of the U.S. Environmental Protection Agency, Robert Stackman of Florida Atlantic University, Amy Wisniewski of the University of Oklahoma Health Sciences Center, Sabra Klein of the Johns Hopkins University Bloomberg School of Public Health, Kim Anderson of Oregon State University, and Gary Wayman of Washington State University. The study was funded by the National Institutes of Health, Autism Speaks and the UC Davis M.I.N.D. Institute.

In addition to Pessah, authors of the Toxicology and Applied Pharmacology study include UC Davis researchers Kyung Ho Kim, Salim Inan and Robert Berman. Inan is currently at the University of Calgary. The study was supported by grants from National Institutes of Environmental Health Sciences, the U.S. Environmental Protection Agency, the UC Davis M.I.N.D. Institute and Science-to- Superfund Basic Research Program.

In addition to Pessah, authors of the Public Library of Science-Biology study included Montserrat Samsó and P.D. Allen of Harvard University's Brigham and Women's Hospital and UC Davis' Wei Feng. The work was supported by the American Heart Association, Brigham and Women's Hospital and the National Institutes of Health.

Story Source:

The above story is reprinted (with editorial adaptations by Science*Daily* staff) from materials provided by **University of California - Davis - Health System**.

said, "and we hope to identify those and help get them off the market."

In addition to Lein and Pessah, authors of the Environmental Health Perspectives study include Dongren Yang (co-first author) of Oregon Health & Science University, Kyung Ho Kim (co-first author) and Andrew Phimister of UC Davis, Adam Bachstetter and Ronald Mervis of the University of South Florida, Thomas Ward and Prasada Kodavanti of the U.S. Environmental Protection Agency, Robert Stackman of Florida Atlantic University, Amy Wisniewski of the University of Oklahoma Health Sciences Center, Sabra Klein of the Johns Hopkins University Bloomberg School of Public Health, Kim Anderson of Oregon State University, and Gary Wayman of Washington State University. The study was funded by the National Institutes of Health, Autism Speaks and the UC Davis M.I.N.D. Institute.

In addition to Pessah, authors of the Toxicology and Applied Pharmacology study include UC Davis researchers Kyung Ho Kim, Salim Inan and Robert Berman. Inan is currently at the University of Calgary. The study was supported by grants from National Institutes of Environmental Health Sciences, the U.S. Environmental Protection Agency, the UC Davis M.I.N.D. Institute and Science-to- Superfund Basic Research Program.

In addition to Pessah, authors of the Public Library of Science-Biology study included Montserrat Samsó and P.D. Allen of Harvard University's Brigham and Women's Hospital and UC Davis' Wei Feng. The work was supported by the American Heart Association, Brigham and Women's Hospital and the National Institutes of Health.

Story Source:

The above story is reprinted (with editorial adaptations by Science*Daily* staff) from materials provided by **University of California - Davis - Health System.**

The researchers found that the two PCBs had different effects. The more potent, PCB95, enhanced the excitability of the brain cells. Researchers were able to decrease this effect by adding a chemical that dampens ryanodine signaling, again implicating the calcium channel as being the key to the disruptions caused by PCBs. The second compound, PCB170, first excited the circuitry, but then the signals returned to baseline because of enhanced inhibition.

These results are significant to the understanding of the potential impact of PCBs on human neurodevelopment, Pessah said.

"We think that in autism, for example, at-risk children have deficient inhibitory circuits. So, if you have a PCB that promotes the excitatory side of the circuit, they would be much more at risk of developing the disorder," he said. "In fact, we chemically blocked inhibitory circuts that unmasked the purely excitotoxic properties of PCB170."

PLoS - Biology study

In the collaborative study between researchers at Davis and Harvard that appears in PLoS-Biology today, researchers showed that PCBs dramatically stabilize the ryanodine receptor in the "on position," which could explain how PCBs are altering brain cell development (as seen in the first study) and altering their excitability (as seen in the second).

"We needed evidence that these compounds directly interact with what we believed to be the target of PCBs," Pessah said.

To that end, the researchers exposed purified ryanodine recptors to PCBs and used electron microscopy to generate extremely high-resolution images of this interaction.

"Our results show that PCB binds directly to ryanodine receptors and locks the channel in the open state, causing mayhem in calcium signaling," Pessah said. This, he added, would account for the effects seen in the first two studies.

"These channels are a target for PCBs, and they are contributing to brain cell dysfunction, even at the behavioral level."

Pessah said that, as early as 1995, he and his colleagues suspected ryanodine receptors were one of the principal targets of PCBs.

"In cellular studies, we couldn't find a way to block the effects of PCBs unless we blocked ryanodine receptors," he said.

Many studies used high doses of PCBs to find subtle or no changes from control. However, in the animal study, Lein actually used both high and low doses. She found that the low-dose group showed more pronounced effects on dendritic growth in the weanling rats than the higher dose.

According to Pessah, the brain has ways of dealing with high levels of toxicity.

"We think that one of the major reasons we have not seen effects in previous studies is that at higher doses PCBs become toxic to cells and the brain has defense mechanisms to deal with disposing of these damaged cells," he said.

These processes, like programmed cell death, would not necessarily be triggered if a neuron's shape is altered rather than damaged, he added. Both Lein and Pessah agreed that the current PCB studies have broader implications for the future study and regulation of PCBs and other environmental toxicants.

Future PCB studies

"Future studies of PCBs and related compounds should be examined at lower doses more relevant to human exposures," Pessah said.

The researchers are planning to study PCB effects on mice that carry some of the same genetic variations of the ryanodine receptors that humans do.

"These studies are important if we are to determine if some people are more susceptible to PCB toxicity than others," Lein said.

The team also will look at PCBs' effects on other ares of the brain that control behavior as well as testing compounds with structures similar to those of PCBs.

"We believe other PCB-like compounds in use today are also capable of changing the structure of protein targets that are contributing to neurobiological problems in humans," Pessah

including ADHD, learning disabilities, sensory deficits, developmental delays and mental retardation

"There is a large body of scientific literature in humans that points the finger at PCBs, linking them to neurodevelopmental problems we see in kids," said Pamela Lein, lead author of the Environmental Health Perspectives animal study and a UC Davis associate professor of molecular biosciences.

"The problem is that it has been difficult to establish a cause-and-effect relationship from the human epidemiological literature without a known mechanism," Lein said. " Now that we have a plausible biological mechanism that could account for neurodevelopmental deficits, we can use the information for diagnosis and for developing potential treatments for PCB exposure."

Environmental Health Sciences study

The study published in Environmental Health Sciences shows that exposure to PCBs in utero and through mothers' breast milk alters a characteristic of neuronal development called dendritic plasticity in young rats. Dendrites are the small, branch-like projections on a neuron that receive signals from other cells in the body. The shape of dendrites changes in response to signaling activity — the phenomenon known as dendritic plasticity. Lein performed the exposure and behavioral studies with colleagues while a researcher at the Johns Hopkins University.

In the study, researchers tried to mimic the low levels of PCB exposure that human children might experience. Experimental rats were fed PCB-laced cookies, while control rats ate normal cookies. Then, when rat pups were weaned from their mothers, they were trained in a water maze to test their ability to use visual cues to learn the location of a platform hidden under the surface of the water. The test has been used in other studies to stimulate dendritic growth, which makes it ideal for measuring effects of toxicants on dendritic plasticity.

The researchers looked at the pattern of dendritic growth in trained and untrained animals from both the control and experimental groups. They found that PCB exposure accelerated dendritic growth in the untrained experimental animals when compared to untrained controls. The trained PCB-exposed animals, however, took longer to learn the water maze and showed reversal of dendritic growth in response to water-maze training. This was in contrast to controls, which showed learning responses and increases in dendritic growth, as predicted by other published studies.

"This tells us that PCBs are altering dendritic growth and plasticity," Lein said.

The results are important because problems in dendritic growth and plasticity have previously been implicated in many neurodevelopmental disorders, including autism, schizophrenia and mental retardation, she said.

"Dendritic plasticity is important to how we process information and, when you perturb that, you interfere with complex behaviors like learning and memory," Lein said.

Pessah and his colleagues showed that brain tissue from untrained rats exposed to PCBs expressed higher levels of the ryanodine receptors.

"We think PCBs are increasing the activity of these calcium channels, which we know generate the signals needed for the extension and branching of dendrites," Pessah said.

He said he believes PCBs lead to overgrowth of dendrites and inhibition of neuronal pruning that takes place during gestational development. Brain cells exposed to PCBs cannot then respond properly to learning.

Toxicology and Applied Pharamacology study

In the study appearing in Toxicology and Applied Pharmacology, Pessah and his colleagues examined the hippocampus, one region of the brain involved in water-maze learning. The researchers measured the excitability of neurons in hippocampal brain tissue of rats before and during exposure to two structurally different PCBs.

Neurons process and transmit information in the form of electrical signals. Their electrical excitability is due to the presence of voltage-sensitive ion channels that directly communicate with ryanodine receptors that reside inside the cell. When excitation is blocked, it is called inhibition. Normal information processing involves a complex balance between excitation and inhibition.

the Calumet ... > *read more*

Exposure To PCBs May Reduce The Effectiveness Of Vaccines In Children (Aug. 22, 2006) — New epidemiological evidence suggests that exposure to environmental pollutants may have an adverse impact on immune responses to childhood vaccinations. The research appears in the Aug. 22, 2006, ... > *read more*

New E-Waste Recycling Technology (Feb. 20, 2007) — With megatons of obsolete personal computers, old cell phones and other waste electrical and electronic equipment piling up every year, scientists in China report development of a much-needed new ... > *read more*

ratify START within days

Tech analyst latest to plead guilty in insider case

Gillette will not renew Tiger Woods

Anarchists claim responsibility for Rome bombs

more top news

Developmental Exposure to Polychlorinated Biphenyls Interferes with Experience-Dependent Dendritic Plasticity and Ryanodine Receptor Expression in Weanling Rats

Dongren Yang,[1] Kyung Ho Kim,[2*] Andrew Phimister,[2] Adam D. Bachstetter,[3] Thomas R. Ward,[4] Robert W. Stackman,[5] Ronald F. Mervis,[3] Amy B. Wisniewski,[6] Sabra L. Klein,[7] Prasada Rao S. Kodavanti,[4] Kim A. Anderson,[8] Gary Wayman,[9] Isaac N. Pessah,[2] and Pamela J. Lein[1,2,10]*

[1]Center for Research on Occupational and Environmental Toxicology, Oregon Health & Science University, Portland, Oregon, USA; [2]Veterinary Molecular Biosciences and Center for Children's Environmental Health, University of California, Davis, California, USA; [3]Neurostructural Research Labs and Center for Aging and Brain Repair, University of South Florida College of Medicine, Tampa, Florida, USA; [4]Neurotoxicology Division, National Health and Environmental Effects Research Laboratory, U.S. Environmental Protection Agency, Research Triangle Park, North Carolina, USA; [5]Department of Psychology, Florida Atlantic University, Boca Raton, Florida, USA; [6]Department of Pediatrics, University of Oklahoma Health Sciences Center, Oklahoma City, Oklahoma, USA; [7]Department of Molecular Microbiology and Immunology, Johns Hopkins Bloomberg School of Public Health, Baltimore, Maryland, USA; [8]Department of Environmental & Molecular Toxicology, Oregon State University, Corvallis, Oregon; USA; [9]Department of Veterinary and Comparative Anatomy, Physiology and Pharmacology, College of Veterinary Medicine, Washington State University, Pullman, Washington, USA; [10]Department of Environmental Health Science, Johns Hopkins Bloomberg School of Public Health, Baltimore, Maryland, USA

BACKGROUND: Neurodevelopmental disorders are associated with altered patterns of neuronal connectivity. A critical determinant of neuronal connectivity is the dendritic morphology of individual neurons, which is shaped by experience. The identification of environmental exposures that interfere with dendritic growth and plasticity may, therefore, provide insight into environmental risk factors for neurodevelopmental disorders.

OBJECTIVE: We tested the hypothesis that polychlorinated biphenyls (PCBs) alter dendritic growth and/or plasticity by promoting the activity of ryanodine receptors (RyRs).

METHODS AND RESULTS: The Morris water maze was used to induce experience-dependent neural plasticity in weanling rats exposed to either vehicle or Aroclor 1254 (A1254) in the maternal diet throughout gestation and lactation. Developmental A1254 exposure promoted dendritic growth in cerebellar Purkinje cells and neocortical pyramidal neurons among untrained animals but attenuated or reversed experience-dependent dendritic growth among maze-trained littermates. These structural changes coincided with subtle deficits in spatial learning and memory, increased [^{3}H]-ryanodine binding sites and RyR expression in the cerebellum of untrained animals, and inhibition of training-induced RyR upregulation. A congener with potent RyR activity, PCB95, but not a congener with negligible RyR activity, PCB66, promoted dendritic growth in primary cortical neuron cultures and this effect was blocked by pharmacologic antagonism of RyR activity.

CONCLUSIONS: Developmental exposure to PCBs interferes with normal patterns of dendritic growth and plasticity, and these effects may be linked to changes in RyR expression and function. These findings identify PCBs as candidate environmental risk factors for neurodevelopmental disorders, especially in children with heritable deficits in calcium signaling.

KEY WORDS: dendrite, neurodevelopmental disorders, developmental neurotoxicity, PCBs, plasticity, ryanodine receptor. *Environ Health Perspect* 117:426–435 (2009). doi:10.1289/ehp.11771 available via *http://dx.doi.org/* [Online 12 September 2008]

Polychlorinated biphenyls (PCBs) are a structurally related group of stable and highly lipophilic chemicals with widespread distribution in the environment (Hornbuckle et al. 2006). Despite being banned in 1977, PCBs persist in the environment, and high residue levels are still detected in human tissues (DeCaprio et al. 2005; Humphrey et al. 2000; Park et al. 2007). Epidemiologic data indicate that PCBs negatively impact neuropsychologic function in exposed children (Carpenter 2006; Korrick and Sagiv 2008; Schantz et al. 2003), and experimental animal studies confirm that developmental PCB exposure causes cognitive and psychomotor deficits (Mariussen and Fonnum 2006). However, the cellular and molecular mechanisms mediating these effects remain speculative.

PCBs interfere with endocrine functions, specifically those mediated by thyroid hormone (Zoeller 2007) and estrogen (DeCastro et al. 2006; Dickerson and Gore 2007), and increase neuronal Ca^{2+} levels via several mechanisms (Kodavanti 2005; Mariussen and Fonnum 2006), including ryanodine receptor (RyR) activation (Pessah and Wong 2001). It is not clear, however, how these molecular effects relate to PCB developmental neurotoxicity. Thyroid hormone (Kapfhammer 2004), estrogen (Cooke and Woolley 2005), and Ca^{2+} (Lohmann and Wong 2005; Redmond and Ghosh 2005) influence neuronal connectivity via dynamic control of dendritic structure. Altered patterns of dendritic growth and plasticity are associated with impaired behavior in experimental models (Berger-Sweeney and Hohmann 1997) and are thought to contribute to diverse neurodevelopmental disorders (Connors et al. 2008; Pardo and Eberhart 2007; Zoghbi 2003), suggesting the possibility that PCBs elicit developmental neurotoxic effects by interfering with neuronal connectivity.

Consistent with this hypothesis, we recently observed that developmental PCB exposure disrupts the balance of neuronal inhibition to excitation in the developing rat auditory cortex (Kenet et al. 2007) and accelerates dendritic growth in the hippocampus and cerebellum of weanling rats (Lein et al. 2007). Questions yet to be addressed include the relationship between PCB interference with neuronal connectivity and known molecular targets of PCBs and whether developmental exposures to PCBs interfere with experience-dependent dendritic plasticity, a phenomenon critical to associative learning and memory (Leuner and Shors 2004). In

Address correspondence to P.J. Lein, University of California Davis, Department of Molecular Biosciences, 1120 Haring Hall, One Shields Ave., Davis, CA 95616 USA. Telephone: (530) 752-1970. Fax: (530) 752-4698. E-mail: pjlein@ucdavis.edu

Supplemental Material is available online at http://www.ehponline.org/members/2008/11771/suppl.pdf

*These authors contributed equally to this work.

We thank L. Calizo, J. Girouard, and B. McKinney for assistance with the Morris water maze; D. Sethajintanin, L. Quarles, and A. Ackerman for congener-specific PCB analyses; and J. Harry and N. Zawia for comments on an earlier version of the manuscript.

The U.S. Environmental Protection Agency approved this work for publication; however, contents do not necessarily reflect the agency's views and policies nor does mention of trade names or commercial products constitute endorsement or recommendation for use.

Support was provided by the National Institutes of Health (HD40936 and NS046649 to P.J.L., 1PO1ES11269 to I.N.P. and GM041292 to G.A.W.), Autism Speaks (I.N.P.), and the UC Davis M.I.N.D. Institute.

The authors declare they have no competing financial interests.

Received 7 June 2008; accepted 11 September 2008.

this study, we used the Morris water maze as a tool for inducing experience-dependent neural plasticity in weanling rats exposed to Aroclor 1254 (A1254) in the maternal diet throughout gestation and lactation. In addition to assessing dendritic morphology in these animals, we also quantified RyR expression and function, thyroid hormone levels, and developmental end points regulated by sex steroids. Our findings suggest that developmental PCB exposure interferes with dendritic growth and plasticity coincident with delayed spatial learning and that perturbation of RyR expression and function contributes to these effects.

Materials and Methods

Detailed descriptions of all methods are available online in Supplemental Material (http://www.ehponline.org/members/2008/11771/suppl.pdf).

Animals and PCB exposures. Animals were treated humanely and with regard for alleviation of suffering according to protocols approved by the Institutional Animal Care and Use Committees of the Johns Hopkins University and Oregon Health & Science University. Adult Long Evans rats were purchased from Charles River Laboratories (Hollister, CA) and housed individually, except during breeding, in standard plastic cages with Alpha-Dri bedding (Shepherd Specialty Papers, Watertown, TN) in a temperature-controlled (22 ± 2°C) room on a 12-hr reverse light–dark cycle. Food and water were provided *ad libitum*. Dams used in the study delivered litters of 10–15 pups (n = 11 dams per treatment group). By postnatal day 2 (P2), litters were culled to five males and five females. Pups were weaned on P21.

Dams were dosed with the commercial PCB mixture Aroclor 1254 (A1254, lot #124-191; AccuStandard, New Haven, CT) at 1 mg or 6 mg/kg/day beginning 2 weeks prior to breeding and continuing until P21. A1254 was diluted in corn oil and pipetted onto one-half of a Keebler Golden Vanilla Wafer (Kellogg Company, Battle Creek, MI). Control animals received wafers dosed with an equal volume (500 µL) of vehicle. Doses were adjusted daily to account for changes in body weight of the dams. Dams were fed the wafers in a separate cage to prevent the pups from accessing the wafers and were watched carefully to ensure that the entire wafer was consumed (typically within 5 min).

Tissue culture and transfection. High-density cultures of dissociated neocortical neurons (10^5 cells/cm^2) were prepared from P1 Sprague Dawley rats (Charles River Laboratories) and maintained in Neurobasal-A (Invitrogen, Carlsbad, CA) supplemented with B27 (Invitrogen) as previously described (Wayman et al. 2006). On day 6 *in vitro* (6-DIV) cultures were transfected with plasmid encoding a microtubule-associated protein-2 (MAP2)-enhanced green fluorescent protein (GFP) fusion construct (Wayman et al. 2006) using Lipofectamine-2000 (Invitrogen) according to the manufacturer's protocol. On 7-DIV, cultures were treated for 48 hr with vehicle (DMSO at 1:1,000 dilution), PCB95 (2,2′,3,5′,6-pentachlorobiphenyl, > 95% purity; AccuStandard), or PCB66 (2,3′,4,4′-tetrachlorobiphenyl, > 95% purity; AccuStandard).

Thyroid hormone assays. Total thyroxine (T_4) and triiodothyronine (T_3) levels were determined in serum samples by radioimmunoassay (Diagnostic Products Corp, Los Angeles, CA) as previously described (Kodavanti et al. 1998).

Analysis of reproductive development. At P2, litter size, sex ratio, and pup body mass were measured. Anogenital distance (AGD) was measured at P2, P10, and P21. At P21, litters were weaned and housed with same-sex siblings. At P40 (puberty), body mass was measured, and the presence of preputial separation or vaginal opening was recorded in males and females, respectively. At P70, blood samples collected from the retro-orbital sinus were analyzed for serum levels of testosterone in males and estradiol in females by radioimmunoassay per the manufacturer's protocol [ICN Biochemicals, Inc. (MP Biomedical, Solon, OH)]. Samples were assayed in triplicate and cross-reactivity with other steroids was < 0.1%. After blood collection, animals were euthanized, and reproductive organs were removed and weighed. The tunica was then stripped from paired testes, and the seminiferous tubules were homogenized in 0.5% Triton-X 100 with 0.01% thimerosal to determine sperm concentration using a Newbauer chamber.

Morris water maze. Spatial learning and memory was assessed on P24 in one male and one female from 11 different litters within each treatment group, using the Morris water maze as previously described (Jett et al. 1997). Rats were tested in one trial per day, except on the first day, when two trials were administered. This modification increases difficulty such that relatively small differences between treatment groups can be detected, yet the task is not too difficult for rats to learn quickly (Jett et al. 1997, 2001; Kuhlmann et al. 1997). An escape latency of 10 sec was chosen as the criterion that animals had learned the task, based on previous studies using rats of comparable age in a similar size pool (Jett et al. 1997, 2001; Markwiese et al. 1998; Rudy et al. 1987). To test spatial memory, a probe test was administered 30 min after the spatial training trials on the first day that the mean escape latency of any treatment group reached criterion.

Morphometric analyses. On P31, animals were euthanized and perfused with 4% paraformaldehyde. To visualize Purkinje cell dendritic arbors, parasagittal cryosections (12 µm) were cut from both cerebellar hemispheres, starting 1 mm from the midline, and reacted with antibody specific for calbindin-D_{28K} (Sigma, St. Louis, MO), which specifically labels Purkinje cells (Christakos et al. 1987). Dendritic arbors of neocortical neurons were visualized by Golgi staining as previously described (Lein et al. 2007). Dendritic arbors were quantified in cultured neocortical neurons transfected with MAP2-eGFP as previously described (Wayman et al. 2006). An average of 10 neurons per culture from three cultures per group was analyzed, and results were confirmed in two independent dissections.

RyR profiling. Specific [^{3}H]-ryanodine (5 nM) binding to whole particulate cerebellar membranes was measured at P21 and P31, as previously described (Wong et al. 1997). Western blot analyses were used to quantify RyR expression as previously described (Roegge et al. 2006).

Cytochrome-P450 (CYP) activity. Hepatic CYP content was determined as previously described (Omura and Sato 1964). 7-Ethyoxyresorufin *O*-deethylase (EROD) and 7-pentoxyresorufin *O*-dependentylase (PROD) activities were analyzed in hepatic microsomes according to the method of Lubet (Lubet et al. 1990) as modified by Kennedy and Kono (Kennedy and Jones 1994; Kono et al. 1999). Enzyme activities were normalized to protein concentration as determined using the BCA Protein Assay (Pierce, Rockford, IL).

Congener-specific PCB analyses. Whole brains from P31 rats were stored at –80°C and thawed immediately before extraction, cleanup, and fractionation using gel permeation chromatography as previously described (Sethajintanin et al. 2004).

Results

Developmental A1254 exposure did not cause maternal or fetal toxicity. Consistent with previous reports (Roegge et al. 2004), dietary exposure of dams to A1254 at 1 mg or 6 mg/kg/day, starting 2 weeks before conception and continuing throughout gestation and lactation, did not negatively impact developmental outcomes or cause overt signs of intoxication in dams or pups as determined by lack of treatment-related changes in maternal weight gain during gestation, maternal body weight during lactation, length of gestation, litter size, and weight gain of offspring during lactation [see Supplemental Material (http://www.ehponline.org/members/2008/11771/suppl.pdf), Figure 1].

Effects of developmental A1254 exposure on thyroid hormone levels and sex steroid-dependent developmental end points. Developmental exposure to A1254 at 1 mg or 6 mg/kg/day

significantly decreased serum concentrations of T_4 and T_3 at P21 (Figure 1). By P31, serum T_3 and T_4 had recovered to control levels among pups in the 1 mg/kg/day A1254 treatment group, but were still significantly depressed in the 6 mg/kg/day treatment group. No sex differences were observed.

As shown in Table 1, developmental A1254 exposure differentially altered a subset of reproductive developmental end points regulated by estrogens and androgens including: *a*) male to female ratio of litters, which was increased in the 6 mg/kg/day A1254 treatment group; *b*) absolute but not relative AGD among female offspring, which was longer than control in both A1254 treatment groups; *c*) vaginal opening, which was significantly delayed among females in the 6 mg/kg/day A1254 treatment group; and *d*) both absolute and relative prostate mass, which was increased in P70 males exposed to A1254 at 1 mg/kg/day but not 6 mg/kg/day, in the maternal diet. A number of other sex steroid–dependent developmental end points were not affected by developmental exposure to either dose of A1254, including AGD (absolute or relative) in males, preputial separation in males, the size of female reproductive organs, the size of male reproductive organs other than the prostate, sperm counts or plasma concentrations of estradiol in females and testosterone in males.

Developmental A1254 exposure alters spatial learning and memory. The Morris water maze has been shown to detect subtle but significant changes in cognitive function in weanling rats exposed to developmental neurotoxicants (Jett et al. 1997, 2001; Markwiese et al. 1998), and training in this task induces experience-dependent dendritic growth (Greenough et al. 1979). Although considered a test of hippocampal function, performance in the Morris water maze is also dependent on the function of the cerebellum and neocortex (Lalonde and Strazielle 2003; Save and Poucet 2000), which is particularly relevant to the current studies because *a*) the vulnerability of the cerebellum to developmental hypothyroidism (Dong et al. 2005) is proposed as a primary mechanism for PCB developmental neurotoxicity (Koibuchi and Iwasaki 2006; Roman 2007; Zoeller 2007); and *b*) our previous studies of molecular biomarkers of dendritic growth (Lein et al. 2007) and development of excitatory to inhibitory balance in neurotransmission (Kenet et al. 2007) indicated that neuronal connectivity in the neocortex may be particularly susceptible to modulation by PCBs.

Training in the Morris water maze was initiated on P24 and concluded on P30 (Figure 2). Repeated-measures two-way ANOVA, with sex and treatment as the between-subjects factors and trial day as the repeated-measures factor, identified a significant interaction between treatment and trial ($p < 0.001$) but a lack of interaction of sex with treatment or trial. There was no three-way interaction among trial, treatment, and sex. Subsequent post hoc Newman-Keuls multiple comparisons on each trial day revealed a significant difference in escape latency between the 1 mg/kg/day treatment group and both vehicle and 6 mg/kg/day treatment groups on day 4. Although significant differences between treatment groups were not detected on other trial days, it is clear from the plot of escape latency that from day 3 through day 7, the 1 mg/kg/day treatment group took longer to find the platform than the control and 6 mg/kg/day treatment group (Figure 2A). The percentage of animals within each treatment group that reached criterion by the end of the training period was significantly reduced in the 1 mg but not 6 mg/kg/day treatment group relative to controls (Figure 2B), further suggesting that weanling rats exposed developmentally to A1254 at 1 mg/kg/day were not as proficient at spatial learning as animals in either the control or 6 mg/kg/day A1254 group. Spatial memory was assessed during the probe test on days 4 and 7, the first day that controls and 1 mg/kg/day–treated animals reached criterion, respectively. On day 4, the 1 mg/kg A1254 rats spent significantly less time in the training quadrant than those from the control or 6 mg/kg/day A1254 groups (Figures 2C and 2E). On day 7, however, there were no significant differences between groups (data not shown), suggesting that although learning and memory were impaired in the 1 mg/kg/day A1254 group, with additional training, rats in this

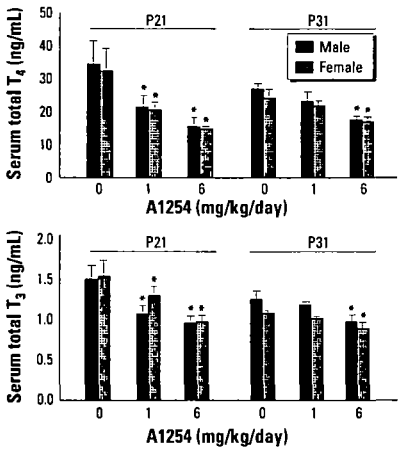

Figure 1. Developmental A1254 exposure decreases serum thyroid hormone levels. Developmental A1254 exposure caused significant dose-dependent decreases in total serum T_4 and T_3 at P21. This effect persisted in the 6 mg but not the 1 mg/kg/day A1254 treatment group at P31. No sex differences were observed. Data are presented as mean ± SEM (n = 7–9/group).
*$p < 0.05$ (two-way ANOVA, with treatment and sex as main effects; Fisher's LSD post hoc).

Table 1. Effects of developmental A1254 exposure on sex steroid-dependent reproductive developmental end points in rats.

	A1254 (mg/kg/day)		
	0	1	6
Male:female ratio[a]	1.05 ± 0.12	1.07 ± 0.22	2.16 ± 0.42*
AGD (mm)[a]			
Male			
P2	3.96 ± 0.14	4.16 ± 0.25	3.93 ± 0.11
P10	7.70 ± 0.26	8.07 ± 0.36	7.76 ± 0.46
P21	16.2 ± 0.53	16.9 ± 0.59	16.9 ± 0.63
Female			
P2	1.98 ± 0.08	2.05 ± 0.19	2.08 ± 0.21
P10	5.14 ± 0.15	5.76 ± 0.21*	5.70 ± 0.27*
P21	9.48 ± 0.29	9.39 ± 0.26*	8.82 ± 0.28*
Puberty (days)[a]			
Males			
Preputial separation	40.36 ± 0.28	40.45 ± 0.14	40.21 ± 0.08
Females			
Vaginal opening	40.05 ± 0.05	40.50 ± 0.19	43.44 ± 1.07*
Adulthood[a]			
Males			
Testes[b] (g)	2.98 ± 0.06	2.95 ± 0.11	3.11 ± 0.03
Epididymal fat pad[b] (g)	3.66 ± 0.13	3.44 ± 0.14	3.31 ± 0.33
Epididymides[b] (g)	0.73 ± 0.03	0.71 ± 0.02	0.69 ± 0.02
Seminal vesicles[b] (g)	0.23 ± 0.01	0.25 ± 0.02	0.23 ± 0.01
Prostate gland[b] (g)	0.49 ± 0.02	0.57 ± 0.03*	0.41 ± 0.01
Testosterone (ng/mL)	5.54 ± 0.87	4.53 ± 0.51	4.40 ± 0.81
Sperm count (× 10^6)	10.40 ± 0.58	9.46 ± 1.15	11.22 ± 0.46
Females			
Ovaries[b] (g)	0.12 ± 0.006	0.13 ± 0.009	0.12 ± 0.004
Ovarian fat pad[b] (g)	4.19 ± 1.04	2.43 ± 0.21	2.19 ± 0.27
Uterine horns[b] (g)	0.29 ± 0.01	0.37 ± 0.05	0.31 ± 0.05
Estradiol (pg/mL)	65.43 ± 6.34	74.80 ± 4.30	68.94 ± 3.57

[a]Mean ± SEM ($n \geq 30$/group). [b]Absolute organ mass. *$p < 0.05$.

group did acquire the task. Developmental exposure to A1254 at either dose had no effect on escape latency in the visual cue test or on swimming speed (Figure 2D), indicating that learning and memory deficits observed in the training trials and probe tests were not due to negative impacts of A1254 on vision, motivation, or swim speed.

Developmental A1254 exposure interferes with dendritic growth and plasticity. Morphometric analyses of Nissl-stained sections indicated no overt treatment-related effects on development of the cerebellum or neocortex [see Supplemental Material (http://www.ehponline.org/members/2008/11771/suppl.pdf), Figure 2]. To assess effects of developmental A1254 exposure on cellular indices of neural circuitry, dendritic length was quantified in individual cerebellar Purkinje cells and neocortical pyramidal neurons at P31. Because no sex differences were observed in PCB effects on performance in the Morris water maze, morphometric studies were restricted to males.

Morphometric analyses of cerebellar neurons immunopositive for calbindin, which is a specific marker of Purkinje cells (Christakos et al. 1987), indicated that among untrained animals, developmental exposure to A1254 at 1 mg but not 6 mg/kg/day significantly increased total dendritic length relative to vehicle controls (Figure 3A). Analysis of the percent change in dendritic length of cerebellar Purkinje cells as a function of maze training within groups revealed that Morris water maze training significantly increased total dendritic length in Purkinje cells of controls, caused significant dendritic retraction in the 1 mg/kg/day A1254 group, and had no significant effect on dendritic length among rats in the 6 mg/kg/day A1254 group (Figure 3B). Comparison between groups indicated that training-induced dendritic growth observed among controls was significantly attenuated by developmental exposure to A1254 at 6 mg/kg/day and actually reversed by A1254 at 1 mg/kg/day (Figure 3B).

Representative camera lucida drawings of the basilar dendritic arbor of neocortical pyramidal neurons from untrained and maze-trained littermates within each group (Figure 3C) demonstrate effects similar to those observed in cerebellar Purkinje cells. Quantification of dendritic length by Sholl analysis indicated that in untrained animals, developmental exposure to A1254 increased dendritic length in neocortical pyramidal neurons by 20% and 17% in the 1 mg and 6 mg/kg/day groups, respectively, relative to controls. Maze training increased dendritic length of neocortical neurons among controls by 22% but caused dendritic length to decrease by 17% in the 1 mg/kg/day A1254 treatment group (Figures 3C and 3D). In animals exposed developmentally to A1254 at 6 mg/kg/day, maze training caused neither significant expansion nor retraction of the dendritic arbor relative to untrained littermates (Figures 3C and 3D). Comparison between groups of the percent change in dendritic length of neocortical pyramidal neurons as a function of maze training indicated that the training-induced dendritic growth observed in controls was inhibited by developmental exposure to A1254, with significantly more pronounced effects observed in the 1 mg versus 6 mg/kg/day A1254 group (Figure 3D).

Developmental A1254 exposure influences RyR profiles. One of the most sensitive molecular targets of PCBs is RyR activation (Pessah and Wong 2001). All three RyR isoforms are expressed in the brain, and RyR activity influences use-dependent synaptic plasticity (Berridge 2006). These observations suggest that PCBs may interfere with dendritic growth and plasticity via RyR-mediated mechanisms. To test this hypothesis, we first determined whether developmental A1254 exposure influenced RyR function and expression. Because the effects of developmental A1254 exposure on dendritic growth

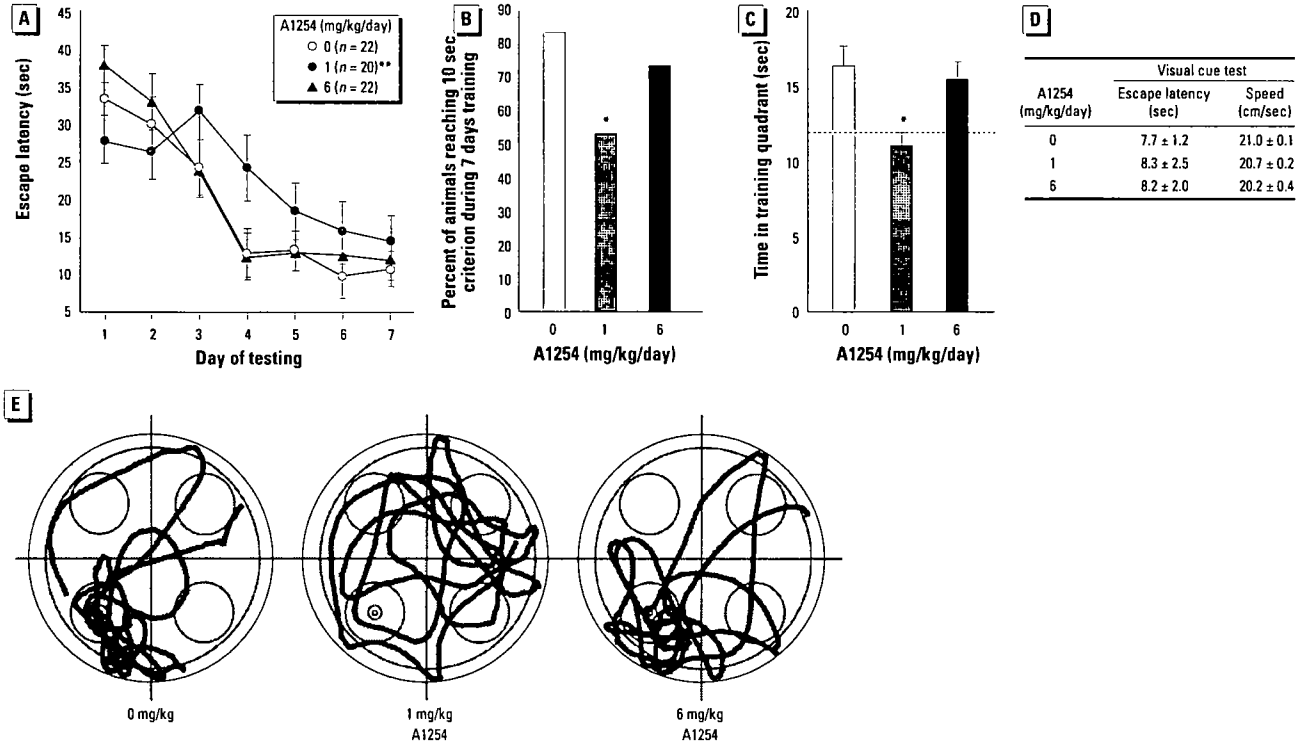

Figure 2. Developmental A1254 exposure at 1 mg but not 6 mg/kg/day impairs performance in the Morris water maze. (*A*) Escape latency as a function of trial. (*B*) Percentage of animals that reached criterion (escape latency ≤ 10 sec) during the 7-day training period. (*C*) Probe tests conducted on day 4. Dotted line indicates predicted time spent in the training quadrant by chance alone. (*D*) Performance in visual cue test and swimming speed. (*E*) Representative swim paths from probe tests on day 4. Data are presented as mean ± SEM.

*$p < 0.05$, **$p < 0.01$ (*A*, repeated measures ANOVA; *B*, Fisher's exact test; *C* and *D*, ANOVA; Newman-Keuls post hoc).

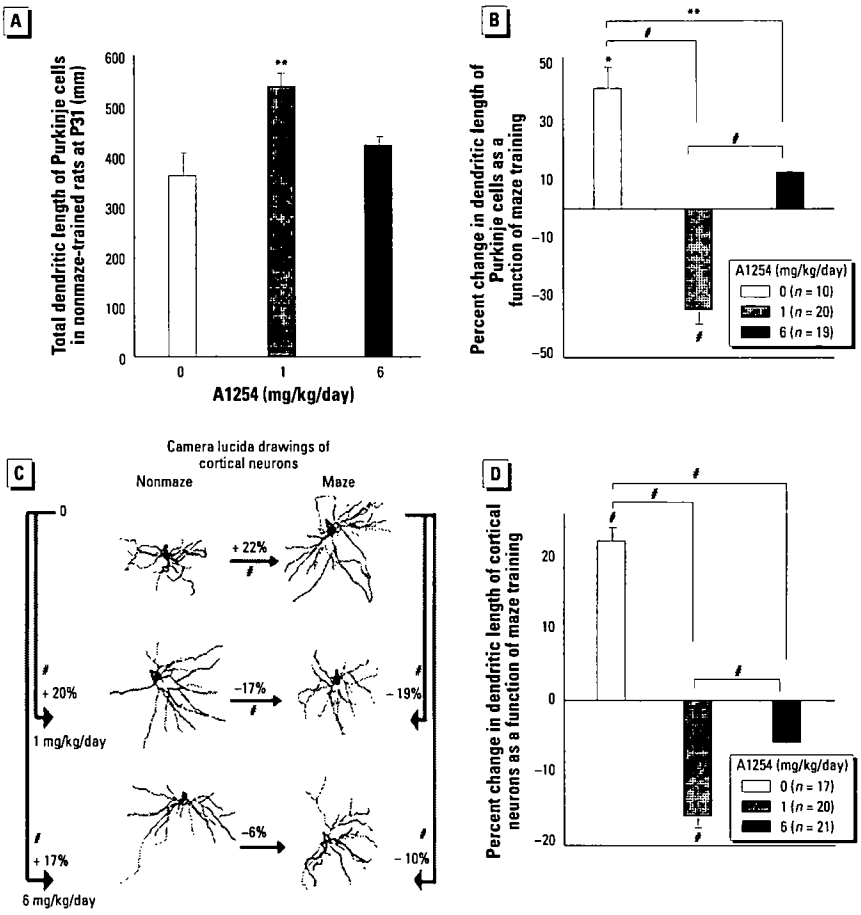

Figure 3. Developmental A1254 exposure interferes with normal dendritic growth and experience-dependent dendritic plasticity. Dendritic morphology was analyzed among P31 rats trained in the Morris water maze (Maze) and among littermates identically housed and exposed but not trained (Nonmaze). (*A*) Total dendritic length of cerebellar Purkinje cells in nonmaze-trained animals. (*B*) Significant effect of maze training on total dendritic length of Purkinje cells. (*C*, *D*) Effects of maze training and developmental A1254 exposure on dendritic growth in cortical neurons. Data are presented as mean ± SEM (n = 17–21 neurons/group). Percent change in dendritic length as a function of maze training was calculated as the difference in dendritic length of neurons in maze-trained animals versus nonmaze-trained animals divided by dendritic length of neurons in maze-trained animals multiplied by 100.
*$p < 0.05$, **$p < 0.01$, #$p < 0.001$ (*A* and *B*, ANOVA followed by Newman-Keuls; *C* and *D*, Wilcoxon test).

and plasticity were similar between cerebellar Purkinje cells and neocortical pyramidal neurons, these studies focused on the cerebellum. To measure the density and level of functional activation of RyR channels, we analyzed specific high-affinity binding of [^{3}H]-ryanodine to membranes prepared from cerebella of males within each group. Scatchard analysis of binding data obtained from cerebellar membranes of P21 animals indicated that developmental A1254 dose-dependently increased the [^{3}H]-ryanodine binding density (B_{max}) without significantly changing apparent affinities (K_D) (Figures 4A and 4B). Comparison of these values to those obtained from [^{3}H]-ryanodine binding to cerebellar membranes isolated from maze-trained P31 rats indicated that maze training did not affect the density of [^{3}H]-ryanodine binding sites measured in controls, but significantly increased the density of functional RyR channels among animals exposed developmentally to A1254 at 1 mg or 6 mg/kg/day, with significantly more pronounced effects observed at the higher dose (Figure 4C).

[^{3}H]-ryanodine binds with high affinity and specificity to all three RyR isoforms and is a measure of the expression levels of functional RyR proteins as well as the stability of the open state of these channels (Buck et al. 1992). To evaluate the effects of developmental A1254 exposure on specific RyR isoforms, we examined expression levels by Western blot using monoclonal antibodies (mAbs) that selectively bind to RyR1 and RyR3 (mAb 34C) or to RyR2 (mAb C3-33) (Airey et al. 1990; Lai et al. 1992). Both RyR1 and RyR2 were observed in cerebellar membranes isolated from P21 and P31 rats, but bands corresponding to the molecular weight of RyR3 were not detected in any sample (Figure 5A). Developmental A1254 exposure increased RyR1 and RyR2 expression levels in the cerebellum of P21 rats (Figure 5B). Although

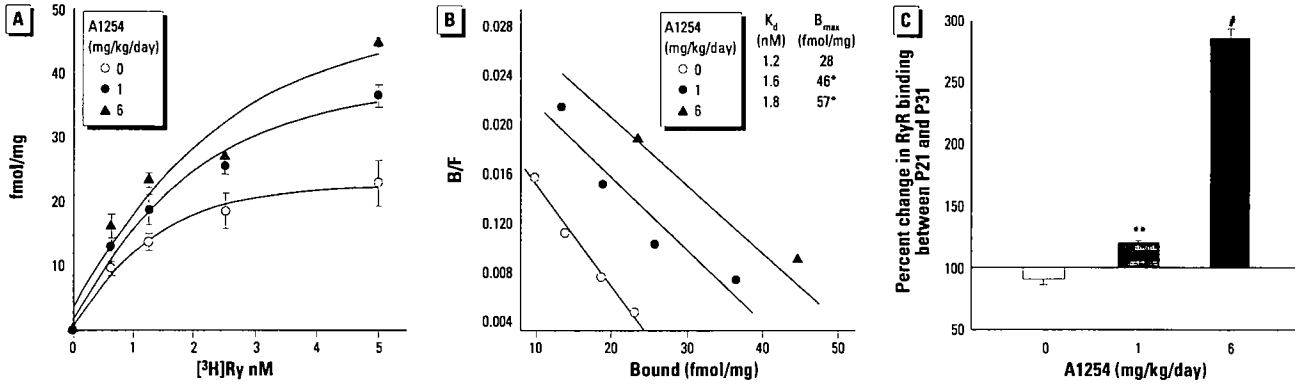

Figure 4. Developmental A1254 exposure increases specific [^{3}H]-ryanodine (Ry) binding to cerebellar membranes. Binding constants (K_d and B_{max}) were determined from a [^{3}H]-ryanodine–binding curve measured in cerebellar membranes from P21 pups (*A*) using Scatchard analysis (*B*). (*C*) Measurements of specific binding of [^{3}H]-ryanodine (5 nM) to cerebellar membranes from P21 and maze-trained P31 rats. The percent change in ryanodine binding between P21 and P31 was calculated as the difference in B_{max} between P21 and P31 divided by B_{max} at P21 multiplied by 100. Data are presented as mean ± SD (n = 4).
*$p < 0.05$, **$p < 0.01$, #$p < 0.001$ (ANOVA; Newman-Keuls post hoc).

the effect on RyR2 expression was similar between A1254 groups, the effect on RyR1 expression was significantly greater in the 1 mg/kg/day A1254 group relative to the 6 mg/kg/day A1254 group. Comparison of cerebellar expression levels of RyR1 and RyR2 between P21 and untrained P31 rats within controls indicated that expression of these RyR isoforms did not increase with age (Figure 5C). As previously reported for RyR2 (Cavallaro et al. 1997), maze training significantly increased RyR1 and RyR2 expression in controls (Figure 5D). In rats exposed developmentally to A1254, maze training also significantly increased RyR2 expression but significantly decreased RyR1 expression (Figure 5D). Comparison between groups of the percent change in RyR1 and RyR2 expression as a function of maze training suggested that developmental A1254 exposure reversed the effects of maze training on RyR1 expression and attenuated the effects of maze training on RyR2 expression; these responses were more pronounced in the 1 mg relative to the 6 mg/kg/day A1254 group.

Congener-specific PCB effects on dendritic growth in cultured neocortical neurons. The observation of similar inverted dose-related effects and training-dependent biphasic responses of dendritic morphology and RyR expression in A1254-exposed animals suggested a causal relationship between these effects. We previously demonstrated that noncoplanar PCBs possessing 2–3 chlorine *ortho* substitutions are the most potent RyR activators (Pessah et al. 2006), consistent with findings from other laboratories that noncoplanar, but not coplanar, PCBs increase intracellular Ca^{2+} in neurons (Kodavanti 2005). Noncoplanar PCBs at nanomolar concentrations interact with RyRs to dramatically increase their sensitivity to activation by nanomolar Ca^{2+} and attenuate their sensitivity to inhibitory feedback by millimolar Ca^{2+} and Mg^{2+} (Pessah and Wong 2001). To further probe the relationship between PCB effects on dendritic growth and RyRs, we quantified dendritic growth in primary cultures of neocortical neurons exposed to individual PCB congeners with differential effects on RyR activity at concentrations that did not adversely influence cell viability in cultured neocortical neurons (Howard et al. 2003). A 48-hr exposure of cultured neocortical neurons (7–9 DIV) to nanomolar concentrations of PCB95, a congener that potently activates RyRs (Pessah et al. 2006), significantly enhanced dendritic growth, whereas exposure to PCB66, a congener with little activity at the RyR (Pessah et al. 2006), had no effect on dendritic growth (Figure 6 A–D). Interestingly, micromolar concentrations of PCB95 had no net effect on dendritic growth compared with controls, recapitulating the

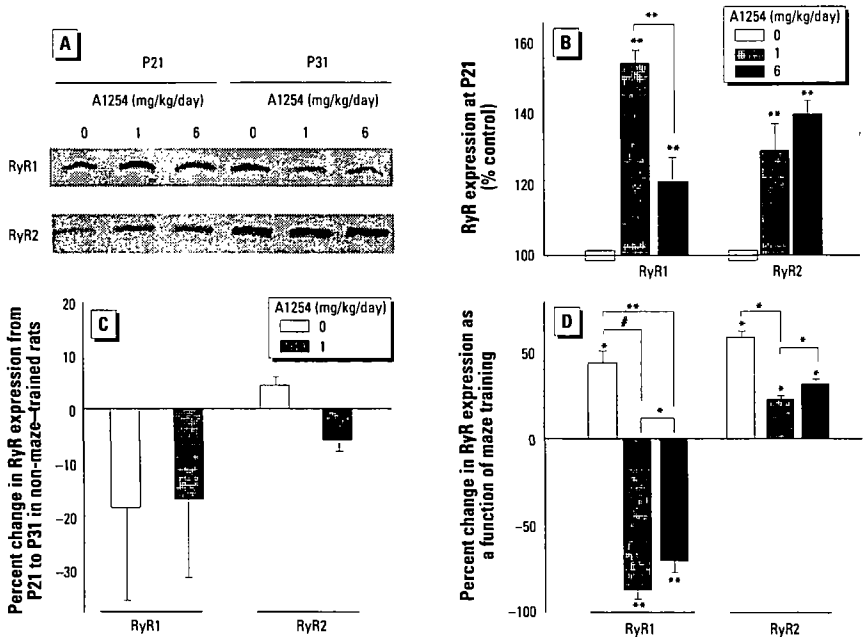

Figure 5. Developmental A1254 exposure alters RyR expression in the cerebellum. (*A*) Representative blot of cerebellar membrane samples from P21 and maze-trained P31 rats probed with RyR antibodies. (*B*) Densitometric analyses of RyR1 and RyR2 expression in the cerebellum at P21. Band densities of samples from A1254-treated animals are plotted as percentage of mean control band densities. (*C*) Cerebellar expression of RyR1 and RyR2 as a function of age in nonmaze-trained animals. Data are presented as percent change in mean pixel density from P21 to P31 within each treatment group. (*D*) Effects of maze training and developmental A1254 exposure on RyR1 and RyR2 expression in the cerebellum. Data are presented as mean ± SEM ($n \geq 4$). Asterisks associated with individual bars indicate statistically significant differences between P21 and maze-trained P31 rats within a group; asterisks above horizontal lines indicate statistically significant difference between groups.
*$p < 0.05$, **$p < 0.01$, $^{\prime}p < 0.001$ (ANOVA; Bonferroni *post hoc*).

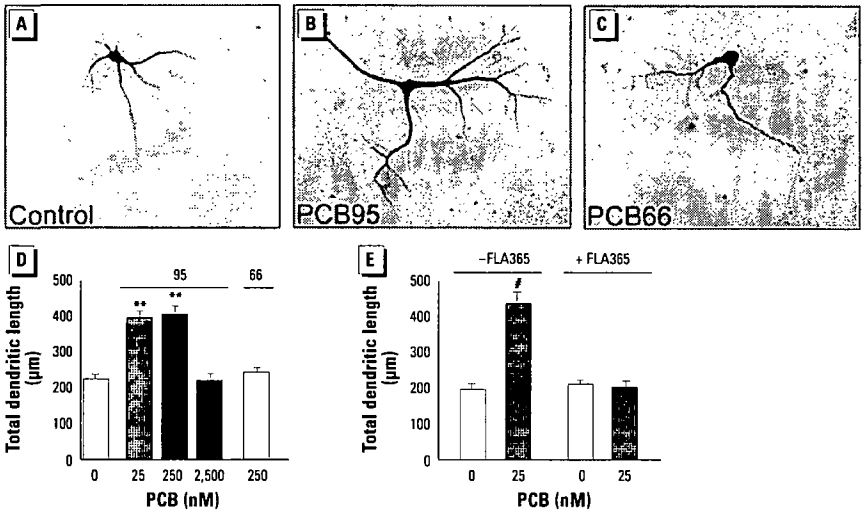

Figure 6. PCB95, but not PCB66, promotes dendritic growth in cultured neocortical neurons. Neurons dissociated from embryonic rat cortices were plated at high density and transfected at 6-DIV with MAP2-GFP, which labels the somatodendritic compartment of 0.5–2% of neurons in the culture. At 7-DIV, cultures were treated with vehicle (0.1% DMSO), PCB66, or PCB95. Photomicrographs of GFP-positive neurons treated with vehicle (*A*), PCB95 (*B*), or PCB66 (*C*) at 250 nM. PCB95, a congener with potent RyR activity, significantly enhanced dendritic growth in cultured cortical neurons in a nonmonotonic fashion (*B, D*). In contrast, PCB66, a congener that lacks RyR activity, had no effect on dendritic growth in cultured cortical neurons (*C, D*). (*E*) PCB95–induced dendritic growth is blocked by the ryanodine receptor antagonist FLA365 (10 μM). Data are presented as mean ± SEM ($n = 30$ neurons/condition).
**$p < 0.01$, $^{\prime}p < 0.001$ (ANOVA; Newman-Keuls post hoc).

inverted dose-related effects of developmental A1254 exposure on dendritic growth *in vivo*. PCB-95–induced dendritic growth was completely blocked in the presence of the selective RyR antagonist FLA365 (Mack et al. 1992) (Figure 6E).

Analyses of PCB levels in weanling rats exposed developmentally to A1254. Our *in vitro* observations strongly suggest that noncoplanar PCB congeners mediated the effects of A1254 *in vivo*. As an indirect test of this hypothesis, we measured CYP activities in hepatic microsomes and quantified levels of individual PCB congeners in the whole brain obtained at P31 from male and female littermates of animals trained in the Morris water maze. Total CYP content was significantly increased by developmental A1254 exposure at P21, but only in the 6 mg/kg/day treatment group, and this effect was no longer evident at P31 (Figure 7A). EROD and PROD activity represent CYP isozymes differentially up-regulated by coplanar and noncoplanar PCBs, respectively (Hansen 1999). Developmental A1254 exposure dose-dependently increased EROD (Figure 7B) and PROD (Figure 7C), and these effects persisted until P31, although the absolute levels of EROD and PROD activity decreased in all treatment groups with increasing age (Figure 7C).

Of the 32 congeners chosen for analysis based on their toxicity, presence in A1254, abundance in environmental samples, and analytical capability, 30 were below the detection limit in brains of controls; the two congeners that were detected, PCB158 and PCB187, were found in only one of four samples (Table 2). In contrast, 14 congeners were detectable in brains from animals in the 1 mg/kg/day A1254 group and 16 in brains from the 6 mg/kg/day A1254 group. These were predominantly *ortho*-substituted, noncoplanar PCBs, and levels were significantly higher in the 6 mg relative to the 1 mg/kg/day A1254 group.

Discussion

The major findings of this study are that developmental PCB exposure enhanced basal dendritic growth but decreased experience-dependent dendritic plasticity, and that these effects correlated better with altered RyR expression than with endocrine disruption.

Developmental A1254 exposure significantly enhanced dendritic growth in cerebellar Purkinje cells and neocortical pyramidal neurons among P31 rats not trained in the Morris water maze, which is consistent with our previous observations that similar exposures accelerated dendritic growth in Purkinje cells and hippocampal CA1 pyramidal neurons between P21 and P60 (Lein et al. 2007). In Purkinje cells, this effect was observed among animals in the 1 mg but not 6 mg/kg/day A1254 group, whereas in neocortical neurons, responses were comparable between A1254 groups. The reason for the different dose–response relationship in different brain regions is not known. Possibilities include regional differences in RyR regulation (Berridge 2006; De Crescenzo et al. 2006; Herrle and Yeckel 2007) or differential upregulation of cytochrome P450 enzymes by AhR ligands in the cerebellum versus neocortex (Iba et al. 2003), which could result in regional differences in PCB toxicodynamics and toxicokinetics, respectively.

Previous studies have shown that experience increases dendritic complexity (Greenough et al. 1979), and we observed that among controls, training in the Morris water maze significantly increased dendritic length in both Purkinje cells and neocortical neurons. However, maze training caused no change in dendritic length in the 6 mg/kg/day A1254 group and significant dendritic retraction in the 1 mg/kg/day A1254 treatment group. Structural plasticity of dendrites is considered the cellular substrate of learning and memory (Leuner and Shors 2004), and we observed that developmental A1254 exposure caused subtle but statistically significant delays in learning and memory that exhibited an inverted dose-related response similar to that observed for experience-dependent plasticity in A1254-treated animals. That these behavioral effects may be of biological significance is suggested by comparison with the human literature, which similarly demonstrates an association between developmental PCB exposures and subtle effects on cognitive function that may be overcome by training or increasing age (Carpenter 2006; Korrick and Sagiv 2008; Schantz et al. 2003). Such subtle effects may have significant biological and social costs when considered at the population level (Grandjean et al. 2007; Weiss 2000).

It is widely postulated that PCB developmental neurotoxicity is mediated by endocrine disruption (Koibuchi and Iwasaki 2006; Roman 2007; Zoeller 2007). Developmental PCB exposure is reported to modulate systemic estrogen levels (Meerts et al. 2004), increase estrogen sensitivity (Ceccatelli et al. 2006), and compete for binding to the estrogen receptor (DeCastro et al. 2006), yet we observed no A1254-related effects on plasma levels of estradiol or testosterone and only minor effects on estrogen- and androgen-dependent developmental end points. The discrepancies probably reflect differences in doses, which were generally much lower in our study, or congener profiles. As previously reported (Crofton et al. 2000; Roegge et al. 2004; Zoeller et al. 2000), developmental A1254 exposure significantly decreased serum thyroid hormone levels. However, it seems unlikely that PCB effects on dendritic growth were due to hypothyroxinemia, because *a*) neonatal hypothyroidism decreases basal dendritic growth (Ruiz-Marcos et al. 1994;

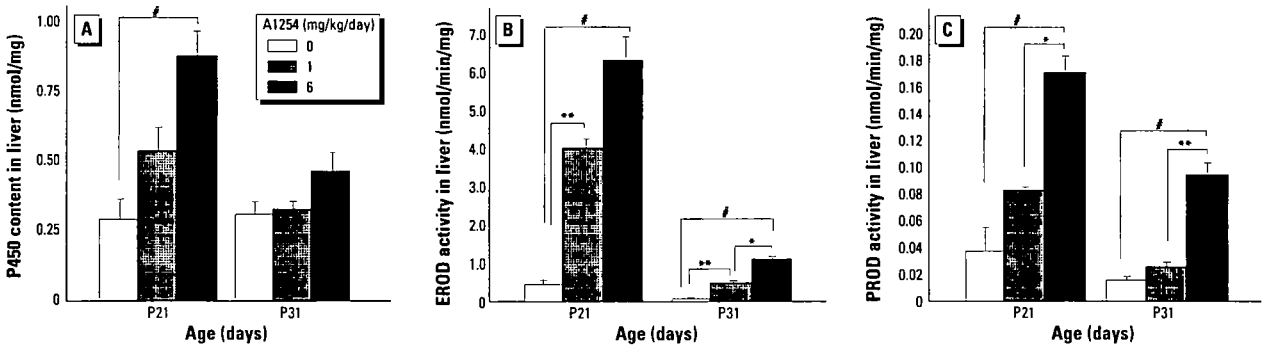

Figure 7. A1254 induction of CYP expression and activity in the liver is dose and age dependent. (*A*) Microsomal CYP content and (*B*) EROD or (*C*) PROD activities were measured in liver at P21 and P31. EROD and PROD were chosen as biomarkers of exposure to coplanar and noncoplanar PCBs, respectively. Liver CYP content was significantly increased relative to controls in the 6 mg/kg treatment group on P21. Developmental A1254 exposure dose-dependently increased EROD and PROD activity at P21 and P31; the increase in PROD activity was significantly different from control only in the 6 mg/kg/day A1254 group. Data are presented as mean ± SEM (n = 5–7/group at P21; n = 10–13/group at P31).
*$p < 0.05$, **$p < 0.01$, $^{\#}p < 0.001$ (ANOVA; Newman-Keuls post hoc).

Uylings et al. 1994), whereas developmental PCB exposure significantly enhanced basal dendritic growth; and *b*) PCB effects on dendritic growth were recapitulated in cultured neocortical neurons removed from systemic thyroid hormone influence. We recently demonstrated that PCB95 significantly disrupts the normal balance of excitatory and inhibitory neurotransmission in the auditory cortex at a dose that has no measurable effect on auditory brain stem responses (ABRs) (Kenet et al. 2007), which is a confirmed T_4-dependent target of PCB (Crofton and Zoeller 2005). Although we cannot preclude the possibility that PCBs influence thyroid hormone signaling downstream of cognate receptors (Zoeller 2007), our data suggest that endocrine disruption is not the sole mechanism underlying PCB effects on neuronal connectivity. Another critical determinant of dendritic morphology is Ca^{2+} signaling (Lohmann and Wong 2005; Redmond and Ghosh 2005). Kodavanti and colleagues (Kodavanti 2005) demonstrated that noncoplanar, but not coplanar, PCBs increase intracellular Ca^{2+} in neurons. Several mechanisms have been shown to mediate this response (Kodavanti 2005; Mariussen and Fonnum 2006), but one of the most sensitive is RyR sensitization (Pessah and Wong 2001). RyR-mediated signals influence neuronal excitability, regulate synaptic plasticity (Collin et al. 2005; Conti et al. 2004; Raymond and Redman 2006; Shimuta et al. 2001), and activate cytosolic (Berridge 2006) and nuclear transcriptional events (Dolmetsch et al. 1998; Li et al. 1998) implicated in activity-dependent dendritic growth (Aizawa et al. 2004; Redmond et al. 2002; Wayman et al. 2006).

Here we show that developmental A1254 exposure dose-dependently increased RyR activity in the cerebellum as determined by [^{3}H]-ryanodine receptor-binding analysis. This is most likely the result of dose-dependent accumulation of PCBs in the brain. The most abundant congeners found in the brain were noncoplanar, which are potent sensitizers of RyR channels (Pessah et al. 2006). One possible consequence of chronic RyR sensitization is altered fidelity of Ca^{2+} signaling (Marks 2002). In our study, elevated [^{3}H]-ryanodine binding was closely associated with differential expression of RyR1 and RyR2 isoforms within the cerebellum, and changes in expression of isoforms were highly dependent on A1254 dose and training status. Interestingly, effects of dose and training on RyR expression closely paralleled their effects on dendritic morphology. Given the fundamental role of RyR in Ca^{2+} signaling and the critical influence of Ca^{2+} signaling on basal and activity-dependent dendritic growth, these data suggest that PCB effects on RyR could be largely responsible for the effects of developmental A1254 exposure on neuronal connectivity observed in weanling rats. In support of this hypothesis, nanomolar concentrations of PCB95, a congener that potently activates RyRs (Pessah et al. 2006), enhanced dendritic growth in primary cultures of neocortical neurons, whereas similar concentrations of PCB66, a congener with negligible effects on RyR activity, had no effect on dendritic growth. Moreover, pharmacologic antagonism of RyR activity blocked PCB95–enhanced dendritic growth. That PCB-mediated RyR dysfunction modulates development of neuronal networks is further supported by our previous demonstration that developmental exposure to PCB95 significantly enhanced the ratio of excitatory to inhibitory currents within the primary auditory cortex (A1) of weanling rats, which was associated with irregularly shaped topographic organization of A1 and disruption of the critical period plasticity that underlies normal postnatal auditory system development (Kenet et al. 2007). It is plausible that these effects reflect changes in basal and activity-driven dendritic complexity, as demonstrated in the present study.

Based on our findings, we propose a novel model of PCB developmental neurotoxicity in which noncoplanar PCBs sensitize RyR activity and alter Ca^{2+}-dependent signaling mechanisms that link neuronal activity to dendritic growth and plasticity. A critical role for RyRs in PCB interference with neuronal connectivity suggests several explanations for the inverted dose-related effects as well as training-dependent biphasic outcomes in dendritic morphology. First, chronic RyR sensitization alters RyR expression, and consequently, downstream Ca^{2+}-dependent events that regulate dendritic growth in an inverted dose-related manner, perhaps because of negative feedback at the higher A1254 dose. Second, intracellular Ca^{2+} promotes dendritic growth in a concentration-dependent manner in early neuronal development (Lohmann and Wong 2005). In later neuronal development, however, moderate increases in Ca^{2+} promote dendritic growth, whereas large increases cause dendritic retraction (Lohmann and Wong 2005; Segal et al. 2000). Thus, increasing PCB doses may increase intracellular Ca^{2+} from concentrations that promote dendritic growth to those that cause dendritic retraction. Furthermore, training-induced increases in intracellular Ca^{2+} superimposed on a background of PCB exposure may push Ca^{2+} concentrations towards those that cause dendrite retraction. Although further studies are required to test these mechanistic hypotheses, the observation of an inverted (or nonmonotonic) dose–response relationship has global regulatory implications as screening and testing programs for endocrine disruption and developmental neurotoxicity that emphasize very high doses of test chemicals with little to no acknowledgement of the importance of nonmonotonic dose–response relationships are finalized (Kimmel and Makris 2001).

The relevance of our findings to human health is suggested by several considerations. First, altered dendritic growth and impaired experience-dependent dendritic plasticity are thought to contribute to the clinical manifestations of various environmentally induced neurodevelopmental disorders in humans (Connors et al. 2008; Pardo and Eberhart 2007; Zoghbi 2003). Second, congener-specific analyses of brains from weanling rats in the 1 mg/kg/day A1254 group identified predominantly *ortho*-substituted congeners

Table 2. Congener-specific analysis of P31 brains.

	PCB (ng/g wet weight)			PCB (ng/g lipid)		
A1254 (mg/kg/day)	0	1	6	0	1	6
Mono-*ortho*[a]						
PCB70	BDL	0.5 ± 0.2	0.6 ± 0.2	BDL	8.8 ± 2.9	11 ± 4
PCB74	BDL	2.0 ± 0.9	2.8 ± 1.3	BDL	36 ± 16	50 ± 24
PCB118	BDL	29 ± 6.1	78 ± 28 **,#	BDL	537 ± 103	1,398 ± 517*,#
PCB105	BDL	11 ± 3.0	23 ± 11*	BDL	199 ± 52	408 ± 208
PCB156	BDL	4.3 ± 1.1*	18 ± 2.0**,#	BDL	80 ± 22*	329 ± 41**,#
PCB189	BDL	BDL	0.8 ± 0.3*	BDL	BDL	14 ± 5*
Di-*ortho*[a]						
PCB99	BDL	22 ± 3.0*	83 ± 10**,#	BDL	398 ± 44*	1,479 ± 200**,#
PCB138	BDL	30 ± 1.1*	133 ± 18**,#	BDL	553 ± 18	2,369 ± 357**,#
PCB153	BDL	22 ± 0.7	110 ± 17**,#	BDL	412 ± 15	1,964 ± 336**,#
PCB128	BDL	5.3 ± 0.8*	10 ± 2.7**,#	BDL	97 ± 13*	171 ± 49**,#
PCB180	BDL	3.4 ± 0.3*	15 ± 2.0**,#	BDL	62 ± 5	275 ± 39**,#
PCB170	BDL	2.8 ± 0.2	13 ± 2.0**,#	BDL	52 ± 4	230 ± 40**,#
PCB158	1.1[b]	3.9 ± 0.2*	14 ± 2.0**,#	23.7[b]	72 ± 5	256 ± 39**,#
PCB166	BDL	BDL	1.3 ± 0.2**,#	BDL	BDL	22 ± 3**,#
Tri-*ortho*						
PCB187	1.0[b]	1.9 ± 0.3*	6.2 ± 0.7**,#	22.6[b]	35 ± 5	111 ± 14**,#
PCB183	BDL	1.0 ± 0.1*	3.7 ± 0.4**,#	BDL	19 ± 3*	66 ± 8**,#

BDL, below the detection limit.
[a]PCB congeners below detection limit in all samples: mono-*ortho*-substituted congeners 8, 28, 60, 66, and 114; di-*ortho*-substituted congeners 44, 49, 52, 82, 87, and 101; non-*ortho*-substituted congeners 37, 77, 126, and 169. Mean ± SEM (n = 4 per group). [b]Concentration detected in one of four samples. *$p < 0.05$ relative to control; **$p < 0.01$ relative to control; #$p < 0.05$ relative to 1 mg/kg/day A1254.

at concentrations ranging from 0.5 ng to 3 ng/g wet weight. Analyses of PCB levels in human brains obtained from the general adult population similarly identified predominantly *ortho*-substituted congeners at concentrations ranging from 0.07 ng to 12 ng/g wet weight (Chu et al. 2003; Covaci et al. 2002; Dewailly et al. 1999). *Ortho*-substituted congeners with the highest activity towards RyRs, including PCB95, collectively represent 40–50% of total PCBs currently found in environmental and biotic samples, and their net effects are likely to be additive (Pessah et al. 2006). Even lower levels of PCB exposure might amplify adverse effects in genetically susceptible individuals (Campbell et al. 2006), particularly if both the genetic factor and PCBs converge to dysregulate the same developmental process. Interestingly, genes that encode Ca^{2+}-regulated signaling proteins involved in synapse formation and dendritic growth are implicated in neurodevelopmental disorders (Krey and Dolmetsch 2007). Considered together, these observations identify PCBs, particularly *ortho*-substituted PCBs with high RyR activity, as candidate environmental risk factors in neurodevelopmental disorders and provide important new clues about the possible role of RyR in contributing to environmentally triggered neurodevelopmental deficits.

References

Airey JA, Beck CF, Murakami K, Tanksley SJ, Deerinck TJ, Ellisman MH, et al. 1990. Identification and localization of two triad junctional foot protein isoforms in mature avian fast twitch skeletal muscle. J Biol Chem 265(24):14187–14194.

Aizawa H, Hu SC, Bobb K, Balakrishnan K, Ince G, Gurevich I, et al. 2004. Dendrite development regulated by CREST, a calcium-regulated transcriptional activator. Science 303(5655):197–202.

Berger-Sweeney J, Hohmann CF. 1997. Behavioral consequences of abnormal cortical development: insights into developmental disabilities. Behavioural brain research 86(2):121–142.

Berridge MJ. 2006. Calcium microdomains: organization and function. Cell Calcium 40(5–6):405–412.

Buck E, Zimanyi I, Abramson JJ, Pessah IN. 1992. Ryanodine stabilizes multiple conformational states of the skeletal muscle calcium release channel. J Biol Chem 267(33):23560–23567.

Campbell DB, Sutcliffe JS, Ebert PJ, Militerni R, Bravaccio C, Trillo S, et al. 2006. A genetic variant that disrupts MET transcription is associated with autism. Proc Natl Acad Sci USA 103(45):16834–16839.

Carpenter DO. 2006. Polychlorinated biphenyls (PCBs): routes of exposure and effects on human health. Rev Environ Health 21(1):1–23.

Cavallaro S, Meiri N, Yi CL, Musco S, Ma W, Goldberg J, et al. 1997. Late memory-related genes in the hippocampus revealed by RNA fingerprinting. Proc Natl Acad Sci USA 94(18):9669–9673.

Ceccatelli R, Faass O, Schlumpf M, Lichtensteiger W. 2006. Gene expression and estrogen sensitivity in rat uterus after developmental exposure to the polybrominated diphenylether PBDE 99 and PCB. Toxicology 220(2–3):104–116.

Christakos S, Rhoten WB, Feldman SC. 1987. Rat calbindin D28K: purification, quantitation, immunocytochemical localization, and comparative aspects. Methods Enzymol 139:534–551.

Chu S, Covaci A, Schepens P. 2003. Levels and chiral signatures of persistent organochlorine pollutants in human tissues from Belgium. Environ Res 93(2):167–176.

Collin T, Marty A, Llano I. 2005. Presynaptic calcium stores and synaptic transmission. Curr Opin Neurobiol 15(3):275–281.

Connors SL, Levitt P, Matthews SG, Slotkin TA, Johnston MV, Kinney HC, et al. 2008. Fetal mechanisms in neurodevelopmental disorders. Pediatr Neurol 38(3):163–176.

Conti R, Tan YP, Llano I. 2004. Action potential-evoked and ryanodine-sensitive spontaneous Ca2+ transients at the presynaptic terminal of a developing CNS inhibitory synapse. J Neurosci 24(31):6946–6957.

Cooke BM, Woolley CS. 2005. Gonadal hormone modulation of dendrites in the mammalian CNS. J Neurobiol 64(1):34–46.

Covaci A, de Boer J, Ryan JJ, Voorspoels S, Schepens P. 2002. Distribution of organobrominated and organochlorinated contaminants in Belgian human adipose tissue. Environ Res 88(3):210–218.

Crofton KM, Kodavanti PR, Derr-Yellin EC, Casey AC, Kehn LS. 2000. PCBs, thyroid hormones, and ototoxicity in rats: cross-fostering experiments demonstrate the impact of postnatal lactation exposure. Toxicol Sci 57(1):131–140.

Crofton KM, Zoeller RT. 2005. Mode of action: neurotoxicity induced by thyroid hormone disruption during development—hearing loss resulting from exposure to PHAHs. Crit Rev Toxicol 35(8–9):757–769.

DeCaprio AP, Johnson GW, Tarbell AM, Carpenter DO, Chiarenzelli JR, Morse GS, et al. 2005. Polychlorinated biphenyl (PCB) exposure assessment by multivariate statistical analysis of serum congener profiles in an adult Native American population. Environ Res 98(3):284–302.

DeCastro BR, Korrick SA, Spengler JD, Soto AM. 2006. Estrogenic activity of polychlorinated biphenyls present in human tissue and the environment. Environ Sci Technol 40(8):2819–2825.

DeCrescenzo V, Fogarty KE, Zhuge R, Tuft RA, Lifshitz LM, Carmichael J, et al. 2006. Dihydropyridine receptors and type 1 ryanodine receptors constitute the molecular machinery for voltage-induced Ca2+ release in nerve terminals. J Neurosci 26(29):7565–7574.

Dewailly É, Mulvad G, Pedersen HS, Ayotte P, Demers A, Weber JP, et al. 1999. Concentration of organochlorines in human brain, liver, and adipose tissue autopsy samples from Greenland. Environ Health Perspect 107:823–828.

Dickerson SM, Gore AC. 2007. Estrogenic environmental endocrine-disrupting chemical effects on reproductive neuroendocrine function and dysfunction across the life cycle. Rev Endocr Metab Disord 8(2):143–159.

Dolmetsch RE, Xu K, Lewis RS. 1998. Calcium oscillations increase the efficiency and specificity of gene expression. Nature 392(6679):933–936.

Dong H, Wade M, Williams A, Lee A, Douglas GR, Yauk C. 2005. Molecular insight into the effects of hypothyroidism on the developing cerebellum. Biochem Biophys Res Commun 330(4):1182–1193.

Grandjean P, Bellinger D, Bergman A, Cordier S, Davey-Smith G, Eskenazi B, et al. 2007. The Faroes statement: human health effects of developmental exposure to chemicals in our environment. Basic Clin Pharmacol Toxicol 102:73–75.

Greenough WT, Juraska JM, Volkmar FR. 1979. Maze training effects on dendritic branching in occipital cortex of adult rats. Behav Neural Biol 26(3):287–297.

Hansen LG. 1999. The Ortho Side of PCBs: Occurrence and Disposition. Boston:Kluwer Academic Publishers.

Hertle DN, Yeckel MF. 2007. Distribution of inositol-1,4,5-trisphosphate receptor isotypes and ryanodine receptor isotypes during maturation of the rat hippocampus. Neuroscience 150(3):625–638.

Hornbuckle KC, Carlson DL, Swackhamer DL, Baker JE, Eisenreich SJ. 2006. Polychlorinated biphenyls in the Great Lakes. In: The Handbook of Environmental Chemistry: Persistent Organic Pollutants in the Great Lakes (Hites RA, ed). Berlin:Springer-Verlag, 13–70.

Howard AS, Fitzpatrick R, Pessah I, Kostyniak P, Lein PJ. 2003. Polychlorinated biphenyls induce caspase-dependent cell death in cultured embryonic rat hippocampal but not cortical neurons via activation of the ryanodine receptor. Toxicol Appl Pharmacol 190(1):72–86.

Humphrey HE, Gardiner JC, Pandya JR, Sweeney AM, Gasior DM, McCaffrey RJ, et al. 2000. PCB congener profile in the serum of humans consuming Great Lakes fish. Environ Health Perspect 108:167–172.

Iba MM, Storch A, Ghosal A, Bennett S, Reuhl KR, Lowndes HE. 2003. Constitutive and inducible levels of CYP1A1 and CYP1A2 in rat cerebral cortex and cerebellum. Arch Toxicol 77(10):547–554.

Jett DA, Kuhlmann AC, Farmer SJ, Guilarte TR. 1997. Age-dependent effects of developmental lead exposure on performance in the Morris water maze. Pharmacol Biochem Behav 57(1–2):271–279.

Jett DA, Navoa RV, Beckles RA, McLemore GL. 2001. Cognitive function and cholinergic neurochemistry in weanling rats exposed to chlorpyrifos. Toxicol Appl Pharmacol 174(2):89–98.

Kapfhammer JP. 2004. Cellular and molecular control of dendritic growth and development of cerebellar Purkinje cells. Prog Histochem Cytochem 39(3):131–182.

Kenet T, Froemke RC, Schreiner CE, Pessah IN, Merzenich MM. 2007. Perinatal exposure to a noncoplanar polychlorinated biphenyl alters tonotopy, receptive fields, and plasticity in rat primary auditory cortex. Proc Natl Acad Sci USA 104(18):7646–7651.

Kennedy SW, Jones SP. 1994. Simultaneous measurement of cytochrome P4501A catalytic activity and total protein concentration with a fluorescence plate reader. Anal Biochem 222(1):217–223.

Kimmel CA, Makris SL. 2001. Recent developments in regulatory requirements for developmental toxicology. Toxicol Lett 120(1–3):73–82.

Kodavanti PRS. 2005. Neurotoxicity of persistent organic pollutants: possible mode(s) of action and further considerations. Dose Response 3:273–275.

Kodavanti PR, Derr-Yellin EC, Mundy WR, Shafer TJ, Herr DW, Barone S, et al. 1998. Repeated exposure of adult rats to Aroclor 1254 causes brain region-specific changes in intracellular Ca2+ buffering and protein kinase C activity in the absence of changes in tyrosine hydroxylase. Toxicol Appl Pharmacol 153(2):186–198.

Koibuchi N, Iwasaki T. 2006. Regulation of brain development by thyroid hormone and its modulation by environmental chemicals. Endocrine J 53(3):295–303.

Kono H, Bradford BU, Yin M, Sulik KK, Koop DR, Peters JM, et al. 1999. CYP2E1 is not involved in early alcohol-induced liver injury. Am J Physiol 277(6 Pt 1):G1259–1267.

Korrick SA, Sagiv SK. 2008. Polychlorinated biphenyls, organochlorine pesticides and neurodevelopment. Curr Opin Pediatr 20(2):198–204.

Krey JF, Dolmetsch RE. 2007. Molecular mechanisms of autism: a possible role for Ca2+ signaling. Curr Opin Neurobiol 17(1):112–119.

Kuhlmann AC, McGlothan JL, Guilarte TR. 1997. Developmental lead exposure causes spatial learning deficits in adult rats. Neurosci Lett 233(2–3):101–104.

Lai FA, Dent M, Wickenden C, Xu L, Kumari G, Misra M, et al. 1992. Expression of a cardiac Ca(2+)-release channel isoform in mammalian brain. Biochem J 288(Pt 2):553–564.

Lalonde R, Strazielle C. 2003. The effects of cerebellar damage on maze learning in animals. Cerebellum (London, England) 2(4):300–309.

Lein PJ, Yang D, Bachstetter AD, Tilson HA, Harry GJ, Mervis RF, et al. 2007. Ontogenetic alterations in molecular and structural correlates of dendritic growth after developmental exposure to polychlorinated biphenyls. Environ Health Perspect 115:556–563.

Leuner B, Shors TJ. 2004. New spines, new memories. Mol Neurobiol 29(2):117–130.

Li W, Llopis J, Whitney M, Zlokarnik G, Tsien RY. 1998. Cell-permeant caged InsP3 ester shows that Ca2+ spike frequency can optimize gene expression. Nature 392(6679):936–941.

Lohmann C, Wong RO. 2005. Regulation of dendritic growth and plasticity by local and global calcium dynamics. Cell Calcium 37(5):403–409.

Lubet RA, Guengerich FP, Nims RW. 1990. The induction of alkoxyresorufin metabolism: a potential indicator of environmental contamination. Arch Environ Contam Toxicol 19(2):157–163.

Mack WM, Zimanyi I, Pessah IN. 1992. Discrimination of multiple binding sites for antagonists of the calcium release channel complex of skeletal and cardiac sarcoplasmic reticulum. J Pharmacol Exp Ther 262(3):1028–1037.

Mariussen E, Fonnum F. 2006. Neurochemical targets and behavioral effects of organohalogen compounds: an update. Crit Rev Toxicol 36(3):253–289.

Marks AR. 2002. Ryanodine receptors, FKBP12, and heart failure. Front Biosci 7:d970–977.

Markwiese BJ, Acheson SK, Levin ED, Wilson WA, Swartzwelder HS. 1998. Differential effects of ethanol on memory in adolescent and adult rats. Alcoholism, clinical and experimental research 22(2):416–421.

Meerts IA, Hoving S, van den Berg JH, Weijers BM, Swarts HJ, van der Beek EM, et al. 2004. Effects of in utero exposure to 4-hydroxy-2,3,3′,4′,5-pentachlorobiphenyl (4-OH-CB107) on developmental landmarks, steroid hormone levels, and female estrous cyclicity in rats. Toxicol Sci 82(1):259–267.

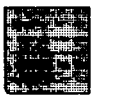

Omura T, Sato R. 1964. The carbon monoxide-binding pigment of liver microsomes. II. Solubilization, purification, and properties. J Biol Chem 239:2379–2385.

Pardo CA, Eberhart CG. 2007. The neurobiology of autism. Brain Pathol 17(4):434–447.

Park JS, Linderholm L, Charles MJ, Athanasiadou M, Petrik J, Kocan A, et al. 2007. Polychlorinated biphenyls and their hydroxylated metabolites (OH-PCBS) in pregnant women from eastern Slovakia. Environ Health Perspect 115:20–27.

Pessah IN, Hansen LG, Albertson TE, Garner CE, Ta TA, Do Z, et al. 2006. Structure-activity relationship for noncoplanar polychlorinated biphenyl congeners toward the ryanodine receptor-Ca2+ channel complex type 1 (RyR1). Chem Res Toxicol 19(1):92–101.

Pessah IN, Wong PW. 2001. Etiology of PCB Neurotoxicity: from molecules to cellular dysfunction. In: Progress In Polychlorinated Biphenyl Toxicology (Robertson L, Hansen L, eds). New York, NY:Academic Press, 179–184.

Raymond CR, Redman SJ. 2006. Spatial segregation of neuronal calcium signals encodes different forms of LTP in rat hippocampus. J Physiol 570(Pt 1):97–111.

Redmond L, Ghosh A. 2005. Regulation of dendritic development by calcium signaling. Cell Calcium 37(5):411–416.

Redmond L, Kashani AH, Ghosh A. 2002. Calcium regulation of dendritic growth via CaM kinase IV and CREB-mediated transcription. Neuron 34(6):999–1010.

Roegge CS, Morris JR, Villareal S, Wang VC, Powers BE, Klintsova AY, et al. 2006. Purkinje cell and cerebellar effects following developmental exposure to PCBs and/or MeHg. Neurotoxicol Teratol 28(1):74–85.

Roegge CS, Wang VC, Powers BE, Klintsova AY, Villareal S, Greenough WT, et al. 2004. Motor impairment in rats exposed to PCBs and methylmercury during early development. Toxicol Sci 77(2):315–324.

Roman GC. 2007. Autism: transient in utero hypothyroxinemia *related to maternal flavonoid ingestion during pregnancy* and to other environmental antithyroid agents. J Neurol Sci 262(1–2):15–26.

Rudy JW, Stadler-Morris S, Albert P. 1987. Ontogeny of spatial navigation behaviors in the rat: dissociation of "proximal"- and "distal"-cue-based behaviors. Behav Neurosci 101(1):62–73.

Ruiz-Marcos A, Cartagena-Abella P, Martinez-Galan JR, Calvo R, Morreale de Escobar G, Escobar del Rey F. 1994. Thyroxine treatment and the recovery of pyramidal cells of the cerebral cortex from changes induced by juvenile-onset hypothyroidism. J Neurobiol 25(7):808–818.

Save E, Poucet B. 2000. Involvement of the hippocampus and associative parietal cortex in the use of proximal and distal landmarks for navigation. Behav Brain Res 109(2):195–206.

Schantz SL, Widholm JJ, Rice DC. 2003. Effects of PCB exposure on neuropsychological function in children. Environ Health Perspect 111:357–576.

Segal M, Korkotian E, Murphy DD. 2000. Dendritic spine formation and pruning: common cellular mechanisms? Trends Neurosci 23(2):53–57.

Sethajintanin D, Johnson ER, Loper BR, Anderson KA. 2004. Bioaccumulation profiles of chemical contaminants in fish from the lower Willamette River, Portland Harbor, Oregon. Arch Environ Contam Toxicol 46(1):114–123.

Shimuta M, Yoshikawa M, Fukaya M, Watanabe M, Takeshima H, Manabe T. 2001. Postsynaptic modulation of AMPA receptor-mediated synaptic responses and LTP by the type 3 ryanodine receptor. Mol Cell Neurosci 17(5):921–930.

Uylings HB, van Pelt J, Parnavelas JG, Ruiz-Marcos A. 1994. *Geometrical and topological characteristics in the* dendritic development of cortical pyramidal and non-pyramidal neurons. Prog Brain Res 102:109–123.

Wayman GA, Impey S, Marks D, Saneyoshi T, Grant WF, Derkach V, et al. 2006. Activity-dependent dendritic arborization mediated by CaM-kinase I activation and enhanced CREB-dependent transcription of Wnt-2. Neuron 50(6):897–909.

Weiss B. 2000. Vulnerability of children and the developing brain to neurotoxic hazards. Environ Health Perspect 108(suppl 3):375–381.

Wong PW, Brackney WR, Pessah IN. 1997. Ortho-substituted polychlorinated biphenyls alter microsomal calcium transport by direct interaction with ryanodine receptors of mammalian brain. J Biol Chem 272(24):15145–15153.

Zoeller RT. 2007. Environmental chemicals impacting the thyroid: targets and consequences. Thyroid 17(9):811–817.

Zoeller RT, Dowling AL, Vas AA. 2000. Developmental exposure to polychlorinated biphenyls exerts thyroid hormone-like effects on the expression of RC3/neurogranin and myelin basic protein messenger ribonucleic acids in the developing rat brain. Endocrinology 141(1):181–189.

Zoghbi HY. 2003. Postnatal neurodevelopmental disorders: meeting at the synapse? Science 302(5646):826–830.

Coordinated Movement of Cytoplasmic and Transmembrane Domains of RyR1 upon Gating

Montserrat Samsó[1*], Wei Feng[2], Isaac N. Pessah[2], P. D. Allen[1]

1 Division of Anesthesia Research, Department of Anesthesia, Perioperative and Pain Medicine, Brigham and Women's Hospital, Harvard Medical School, Boston, Massachusetts, United States of America, **2** Department of Molecular Biosciences, School of Veterinary Medicine, University of California, Davis, Davis, California, United States of America

Ryanodine receptor type 1 (RyR1) produces spatially and temporally defined Ca^{2+} signals in several cell types. How signals received in the cytoplasmic domain are transmitted to the ion gate and how the channel gates are unknown. We used EGTA or neuroactive PCB 95 to stabilize the full closed or open states of RyR1. Single-channel measurements in the presence of FKBP12 indicate that PCB 95 inverts the thermodynamic stability of RyR1 and locks it in a long-lived open state whose unitary current is indistinguishable from the native open state. We analyzed two datasets of 15,625 and 18,527 frozen-hydrated RyR1-FKBP12 particles in the closed and open conformations, respectively, by cryo-electron microscopy. Their corresponding three-dimensional structures at 10.2 Å resolution refine the structure surrounding the ion pathway previously identified in the closed conformation: two right-handed bundles emerging from the putative ion gate (the cytoplasmic "inner branches" and the transmembrane "inner helices"). Furthermore, six of the identifiable transmembrane segments of RyR1 have similar organization to those of the mammalian Kv1.2 potassium channel. Upon gating, the distal cytoplasmic domains move towards the transmembrane domain while the central cytoplasmic domains move away from it, and also away from the 4-fold axis. Along the ion pathway, precise relocation of the inner helices and inner branches results in an approximately 4 Å diameter increase of the ion gate. Whereas the inner helices of the K^+ channels and of the RyR1 channel cross-correlate best with their corresponding open/closed states, the cytoplasmic inner branches, which are not observed in the K^+ channels, appear to have at least as important a role as the inner helices for RyR1 gating. We propose a theoretical model whereby the inner helices, the inner branches, and the h1 densities together create an efficient novel gating mechanism for channel opening by relaxing two right-handed bundle structures along a common 4-fold axis.

Citation: Samsó M, Feng W, Pessah IN, Allen PD (2009) Coordinated movement of cytoplasmic and transmembrane domains of RyR1 upon gating. PLoS Biol 7(4): e1000085. doi:10.1371/journal.pbio.1000085

Introduction

Maintaining a precise intracellular Ca^{2+} concentration that is 10,000-fold lower than the surrounding environment of the cell, and the ability to dramatically increase intracellular calcium to trigger downstream events in response to specific stimulus are key for cell survival [1]. Ryanodine receptors (RyRs) are high-conductance intracellular Ca^{2+} channels regulated by both exogenous and intracellular mediators, which release Ca^{2+} stored in the endoplasmic reticulum. RyRs are the largest ion channels known, with an average molecular weight of 2.26 MDa, with most of its mass (~4/5) forming the cytoplasmic domain. The skeletal muscle isoform, RyR1, has a bidirectional interaction with the slow voltage-gated calcium channel in the cell membrane, or dihydropyridine receptor (DHPR), which acts as RyR1's voltage sensor for cell membrane depolarization [2]. Two key questions to understand RyR1's function are how are signals transmitted from peripheral cytoplasmic domains to the ion gate, and what is the gating mechanism itself.

Cryo-electron microscopy (cryoEM) and single-particle image analysis of frozen-hydrated RyR1 revealed the 3D structure of RyR1 at approximately 25–30 Å resolution [3–5]. Its cytoplasmic domain is shaped like a flat square prism of 290 Å side and 120 Å high, with at least 12 reproducible domains that have been assigned numerals 1–12 [6,7]. Using the same technique, it has also been possible to map the binding sites for several ligands: the FK506-binding protein 12 kDa (FKBP12), calmodulin (Ca^{2+}-CaM, apoCaM), and imperatoxin A (IpTxA) [8–10]. All these interactions, which are known to modulate RyR1 gating, take place at distances at least 130 Å away from RyR1's putative ion gate and suggest that RyR1 makes use of long-range allosteric pathways between the cytoplasmic sensing domains and the ion gate. The 3D reconstructions of RyR1 in the open conformation indicated several conformational changes involving both the cytoplasmic and transmembrane domains with respect to the closed conformation [11,12]; however, the resolution of these reconstructions (~30 Å) is insufficient to understand the connection between the two domains or to distinguish the substructure within the transmembrane domain itself.

The wealth of atomic structures of K^+ channels solved by X-ray crystallography obtained in the last decade has allowed

Academic Editor: Richard W Aldrich, University of Texas Austin, United States of America

Received December 15, 2008; **Accepted** March 3, 2009; **Published** April 14, 2009

Abbreviations: BLM, bilayer lipid membrane; CaM, calmodulin; cryoEM, cryo-electron microscopy; DHPR, dihydropyridine receptor; FKBP12, FK506-binding protein 12 kDa; IpTxA, imperatoxin A; nAChR, nicotinic acetylcholine receptor; RyR, ryanodine receptor; SR, sarcoplasmic reticulum

* To whom correspondence should be addressed. E-mail: msamso@zeus.bwh.harvard.edu

Author Summary

Maintaining a precise intracellular calcium concentration is key for cell survival. In skeletal muscle, ryanodine receptor type 1 (RyR1) is an intracellular calcium-release channel that is critical for contraction. Here, we used single-channel techniques to demonstrate the presence of functionally homogenous populations of RyR1 in either the closed or open state and then applied cryo-electron microscopy and image processing to determine the 3D structure of each state. The 3D structures show that RyR1's ion pathway is formed by two sets of bundles, each containing four rods along a common axis. One set (inner helices) stretches from the lumen to the ion gate, whereas the second (inner branches) stretches from the ion gate to the peripheral cytoplasmic domains. The configuration of the two bundles is clearly different in the two physiological states, allowing a 4 Å increase in diameter of the ion gate upon opening. This diameter increase is sufficient to ensure flow of calcium ions. Upon gating, the cytoplasmic domains undergo a conformational change that converges on the inner branches, revealing a long-range allosteric mechanism that directly connects effectors acting on the cytoplasmic moiety with the ion gate.

extensive study of the structural rearrangements underlying ion gating for this channel family. In the prevalent model for the ion gating of the K^+ channel, the inner helices bend outwards around their midpoint (through a Gly or a Pro-X-Pro hinge) to increase the diameter of the ion gate so that it becomes permeable to ion flow. These inner helices are connected to their sensing domains using a plethora of structural arrangements to respond to a variety of effectors (voltage, ion concentration, pH, redox state, small molecules, and ligands). However, with one exception [13], models of K^+ channel gating have been deduced from comparison of unrelated K^+ channels. The only other case in which structural data at near-atomic detail is available for both the open and closed states in the same channel is for the nicotinic acetylcholine receptor (nAChR), as determined by electron crystallography [14]. Unlike other K^+ channels, the nAChR is a pentamer with its ion gate formed by a hydrophobic girdle in the middle of the membrane. Binding of acetylcholine induces a rotation in protein chains that communicates to the inner helices of the pore, resulting in modulation of the ion gate diameter. To date, nothing is known about the ion gating mechanism of RyR1.

Using cryoEM, we previously defined the architecture of RyR1's transmembrane domain in the closed state at higher detail [7]. RyR1's closed ion pore is defined by an axial structure formed by two sets of four rods each forming a right-handed bundle, which we defined as the inner helices, and the inner branches. The inner helices shape the core of the transmembrane assembly. The inner branches are in the center of the cytoplasmic assembly and are directly connected with the peripheral cytoplasmic domains. The two bundles converge into a ring of high density, which we presumed to be the ion gate. A second constriction, which would correspond to the selectivity filter, is on the sarcoplasmic reticulum (SR) luminal side of the transmembrane assembly. These two constrictions define a central cavity. The structure formed by RyR1's inner helices in the closed state appears to be parallel to the canonic structure of the inner helices of closed K^+ channels [15,16]. A second group of investigators has also reported the presence of the inner helices in the core of the transmembrane assembly of RyR1 in the closed state, achieving similar resolution using the same method and almost identical biochemical conditions [17]. Intriguingly, the conformation that they reported for the inner helices corresponded best to that of an open K^+ channel, and suggested that the ion gating mechanism used by RyR1 must be radically different than that used by K^+ channels.

To better understand the basis for RyR1's gating and to solve the controversy on the conformation of the inner helices in the closed state, we sought to obtain the open and closed conformations of RyR1 in their (frozen) hydrated state using single-particle cryoEM. Furthermore, we used single-channel biophysical characterization of the two states in bilayer lipid membranes (BLMs) using identical samples and conditions, to have a more direct correspondence between conformation and biophysical state of the channel. Here, we present the first demonstration, to our knowledge, of a midlevel resolution 3D model for the open state of RyR1 bound to its accessory protein FKBP12. A 3D reconstruction of RyR1-FKBP12 in the closed state was obtained in parallel for comparison. Thus, in this study, we are able to directly compare both conformations of the same protein, rather than comparing related proteins. Furthermore, both structures correspond to the protein in its fully hydrated state, and both are correlated directly to a functionally characterized biophysical state. We found that upon opening, the cytoplasmic domain undergoes an overall conformational change that involves the connections with the transmembrane domain. In the transmembrane assembly, we find that the inner helices corresponding to the open and closed states of RyR1 have a high cross-correlation with parallel structures of K^+ channels in the corresponding state. Nevertheless, the ion pathway of RyR1 has features not present in K^+ channels, which has allowed us to create a novel heuristic model for RyR1's ion gating.

Results

Stabilizing Open and Closed States in RyR1

To obtain the resolution necessary for the visualization of secondary structure (~9 Å), it is critical to obtain a highly homogeneous dataset. Obtaining a homogeneous population of RyR1 in the closed state is relatively easy. By contrast, the typical flickering behavior of RyR1 under physiologic activating conditions represents a significant limitation, since it produces a mixed population of open and closed states, e.g., under maximum Ca^{2+} activating conditions (50 μM Ca^{2+} on the cytoplasmic side), the channel open probability (P_o) of reconstituted purified RyR1-FKBP12 channels is less than 30% (unpublished data). Our previous studies using vesicles demonstrated that the neuroactive noncoplanar polychlorinated biphenyl 2,2′,3,5′,6-pentachlorobiphenyl (PCB 95) had an unprecedented activating effect on RyR1 [18,19], suggesting that it would be a candidate small molecule to stabilize RyR1's open state. The BLM studies of reconstituted purified RyR1-FKBP12 channels indicate that PCB 95 stabilizes the full open (conducting) state in ten out of ten reconstituted channels, resulting in extremely long-lived openings interspersed with rare short-lived transitions to the closed state. This results in a mean P_o of 0.96 and thus produces a highly homogeneous dataset (Figure 1C–1E). By contrast, addition of

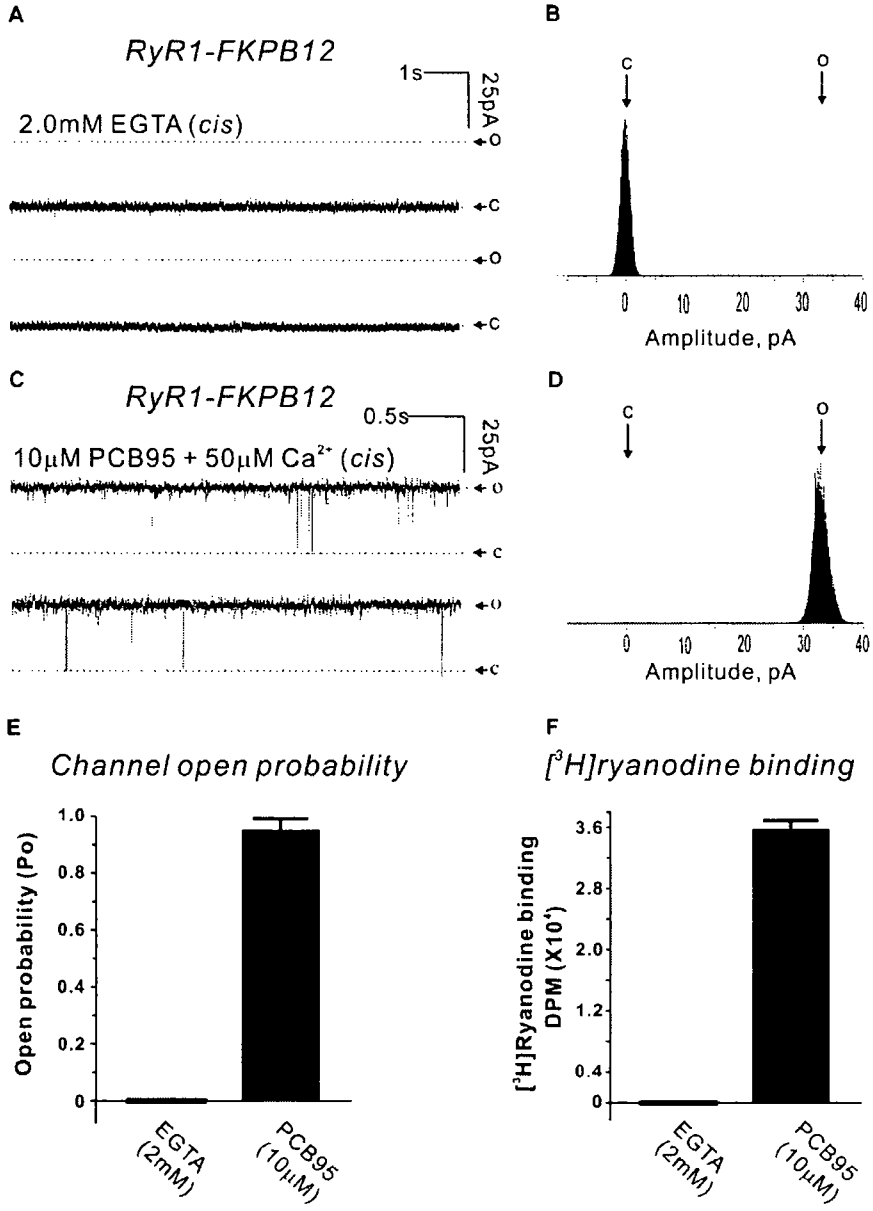

Figure 1. Creating Functionally Homogeneous Open and Closed Datasets of RyR1-FKBP12

(A–E) Purified RyR1 channels were reconstituted in BLMs from a total of four independent junctional SR preparations. Once channels were fused and verified for activity, 2 mM EGTA ($pCa^{2+} < 10^8$) perfused into the *cis* chamber produced a fully closed state (C) with no gating transitions to the open state (O) as shown by the BLM traces and amplitude histogram of the representative channel (A and B). This behavior was observed in four of four channel reconstitutions (E). Pretreatment with PCB 95 (10 μM) persistently stabilized the full open state of RyR1 as shown by the representative channel (C and D). The *cis* solution contained 50 μM Ca^{2+}, 10 μM PCB 95, and 100 nM FKBP12 throughout the recording. This behavior was observed in ten of ten reconstitutions (E) and lasted the duration of each recording (ranging between 12 s and 6 min).

(F) [^{3}H]ryanodine binding to RyR1 junctional SR vesicles in the presence of 2 mM EGTA show negligible specific high-affinity binding or in the presence of 50 μM free Ca^{2+} and 10 μM PCB 95 shows $>3.5 \times 10^4$ dpm specific binding. The data summarize results from four independent measurements obtained from two different junctional SR preparations.

doi:10.1371/journal.pbio.1000085.g001

2 mM EGTA to the *cis* chamber ($pCa^{2+} < 10^8$) after fusion of an actively gating channel completely stabilized the fully closed state of the channel with no gating transitions observed for the entire recording period ($P_o = 0$) (Figure 1A, 1B, and 1E). High-affinity [^{3}H]ryanodine binding experiments query the conformational state of a large number of RyR1s [20]. The presence of EGTA (2 mM) in the assay buffer negates specific binding of [^{3}H]ryanodine because the channels are in a closed conformation. By contrast, the presence of PCB 95 and optimal Ca^{2+} produced nearly 10 pmol of binding sites per milligram of SR protein (~35,000 disintegrations per minute [dpm]/25 μM of SR protein) at steady state (Figure 1F), indicative of the fact that the channels are stabilized in the open state. These biophysical and biochemical data provide two independent measures of the ability of PCB 95 to stabilize the open state of the RyR1

channel having a unitary current level indistinguishable from a native channel in the full open state. The unitary current is a fundamental parameter for any given channel [21], thus it is safe to assume that the PCB 95–stabilized RyR1 has a pore structure representative of the native open state (in which only the kinetic/thermodynamic parameters have been altered). To exert its effect, PCB 95 requires that RyR1's FKBP12 accessory subunit be bound [22]. In vivo, FKBP12 is constitutively bound to RyR1 and is known to stabilize its fully closed state and minimize subconductance states [23,24]. Both the position and orientation of FKBP12's atomic coordinates with respect to RyR1 have been mapped and have been shown not to alter RyR1's closed-state conformation at 16 Å resolution [9].

Cryo-Electron Microscopy of RyR1

Our RyR1 purification method [7] produced a single band on PAGE (Figure 2A) indicative of a pure RyR1 preparation, and RyR1s with well-preserved structure when viewed with cryoEM (Figure 2B). The relatively high concentration of RyR1, approximately 2 mg/ml, enabled the successful cryo-preparation of RyR1 suspended over holes instead of lying on a carbon support, a method that allows increased resolution of the 3D reconstruction because it considerably increases the randomness of orientations [7]. CryoEM and image processing of two frozen-hydrated RyR1-FKBP12 datasets corresponding to the open and closed states, with approximately 17,000 particles each, yielded two 3D reconstructions. The homogeneous angular distribution for both datasets (Figure 2C) indicates that all orientations are equally represented in both datasets; thus the two 3D reconstructions have isotropic resolution and are free of the missing-cone artifact [25]. The nominal resolution of the two reconstructions, 10.2 Å, was determined by Fourier shell correlation (FSC) using a cutoff criterion of 0.143 [26] (Figure 2D), which in this study was a conservative value relative to the five times noise-correlation cutoff. The resolution value of 10.2 Å appears reasonable, taking into account the fact that in general, positive identification of secondary structure is indicative of 9 Å or better resolution. We have focused our analysis on only those structures readily visible in the cryoEM density map without any further manipulation. Specifically, we have centered our study on structures with densities at least 2.8 σ levels above the mean value.

Ion Gate Opening Mechanism: Conformational Changes in the Cytoplasmic Assembly

When comparing the 3D reconstructions corresponding to closed and open RyR1, they look rather similar (Figure 3). However, careful analysis reveals that they are different conformomers of the same molecule. The coarse conformational changes may be better appreciated when the two 3D reconstructions are filtered to lower resolution and directly superimposed (Figure 4A), or when the two 3D structures alternate between the closed and open states (Video S1). Whereas most of the domains appear to move, the largest conformational changes take place in the distal regions of the cytoplasmic domains. The larger conformational changes are also evident in the 3D difference maps (Figure 4B). The difference was performed in both directions (closed minus open, and open minus closed), providing the regions of mass that were exclusive for the closed and open states, respectively.

Because the open- and closed-state datasets were processed in parallel, starting from a common low-resolution structure, and result in clearly different conformations, we believe that these are genuine representations of the two physiological states. Furthermore, given the large dimensions of the RyR1 (e.g., 30× larger than the K^+ channel KcsA), domains separated by more than 100 Å may be regarded as resolved independently from each other. Yet, these domains follow the same direction of movement when they are connected by intervening density. Finally, for each domain that moved, there is a pair of complementary differences (see Figure 4B), which is also indicative of high data quality and actual movement.

The largest-magnitude conformational change occurs in the cytoplasmic domain, whereby each of the quadrants swivels outwards. The corners or clamp domains (domains 9 and 10) together with the structure formed by domains 7, 8, and 8a move away from the T-tubule and towards the SR membrane by approximately 8 Å. Concomitantly, domain 2, more central and facing the T-tubule, moves approximately 4 Å towards the T-tubule, and outwards away from the 4-fold axis (Figure 4A). We do not see an opening of the clamp domains in the open state as was suggested previously (see Discussion). Domain 6, protruding towards the T-tubule, moves approximately 5 Å outwards when the channel is in the open state, and a similar magnitude of outward movement takes place at domain 11, facing the SR membrane. The main effect of this swiveling movement is that the mass moves from the center to the outside, making the 4-fold axis less crowded. This movement in the cytoplasmic regions is clearly conveyed to the inner branches (Figure 3A and 3C, Video S1).

A Reproducible Model of RyR1's Ion Pathway

In the closed state, the overall structure of the inner helices and inner branches of RyR1-FKBP12 display a structure almost identical to the structure of the closed state of RyR1 that we determined previously in the absence of FKBP12 [7] (compare Figures 3B, 3D, and 5A). As in our earlier report, the inner helices have a tepee-like arrangement that overlaps directly with the tepee structure described for the ion pathway in the atomic models of K^+ channels [15,16,27–29] (e.g., see Figure 6). Although a resolution of 9 Å or better is needed to visualize α helices [30,31], it has been described that resolution of 10 Å or even less may suffice to identify α helices, if they are separated from surrounding structures [32]. Another report of the closed state of RyR1 at 10 Å [17] also indicated four inner helices in the same location—although in a different configuration—supporting this finding (Figure 5B). When compared to our closed-state reconstruction, the inner branches in the open state are clearly recognizable but in a different conformation, and the central passage has significantly lower density than in the closed state (stereo pairs shown in Figures 3B and 5A). The inner branches and inner helices define three main constrictions along the 4-fold axis, represented in Figure 7. The upper, or cytosolic, constriction is defined by the distal enlargement of the inner branches (Figure 7A). The meeting point between the inner branches and the inner helices defines the ion gate (Figure 7B). The lowest constriction defines the opening to the SR lumen (Figure 7C), and is formed by the pore helices in a region that corresponds to the selectivity filter of the K^+ channels. The inner helices, the ion gate, and the putative

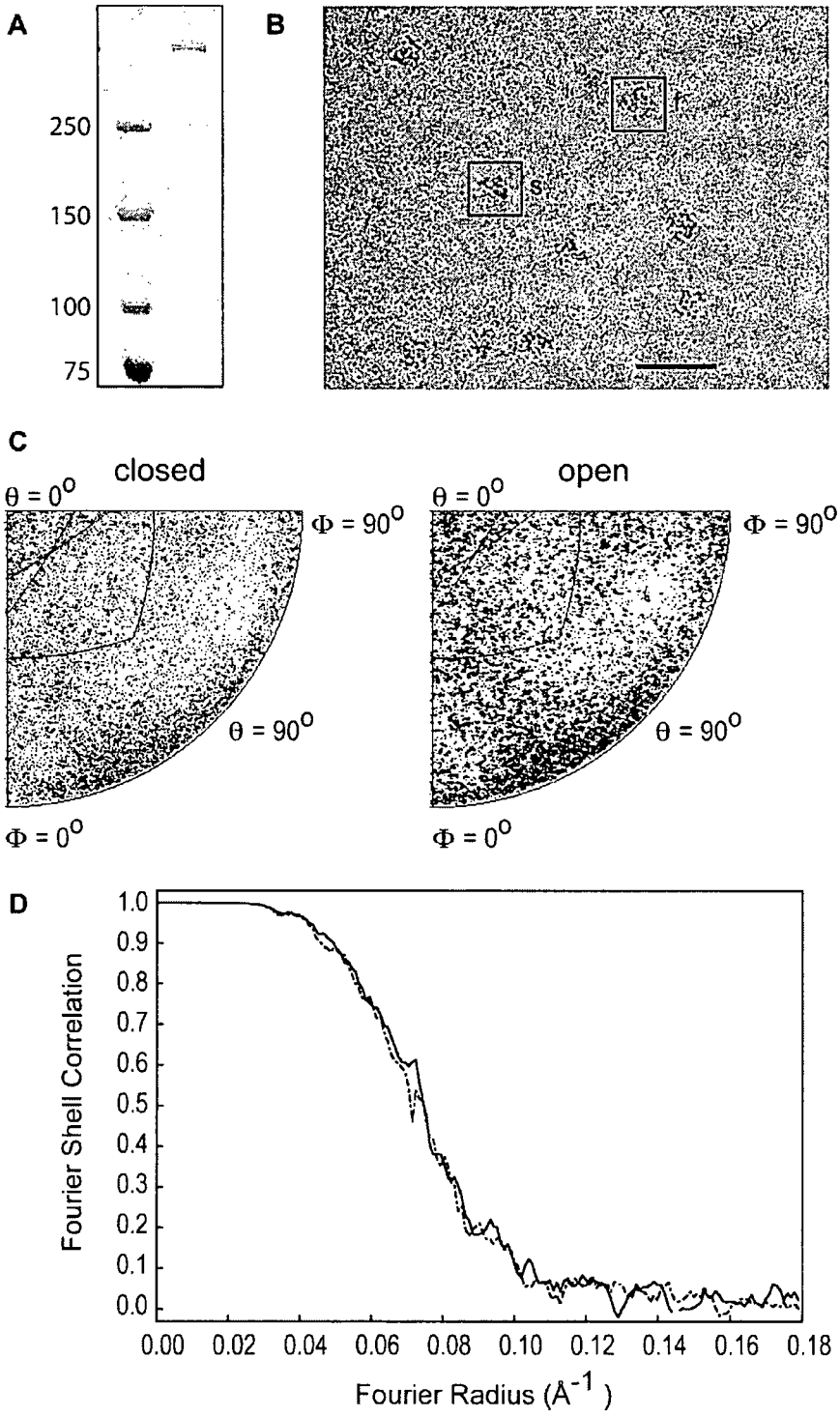

Figure 2. Biochemistry, Cryo-Electron Microscopy, and Single-Particle Image Processing

(A) SDS-PAGE of purified RyR1 (right lane) with molecular weight markers on the left.

(B) Electron microscopy of a field of RyR1 particles embedded in ice, with the particles showing clear substructure. A 4-fold view and a side view are highlighted with the letters f and s, respectively. Scale bar indicates 100 nm.

(C) Plots of the angular distributions of the particles used in the 3D reconstructions in the closed and open conformations, showing a uniform distribution of Euler angular orientations of the vitrified RyR1.

(D) The Fourier shell correlation curves indicate 10.2 Å resolution for the closed (continuous line) and open (dashed line) datasets according to the 0.143 cutoff criterion.

doi:10.1371/journal.pbio.1000085.g002

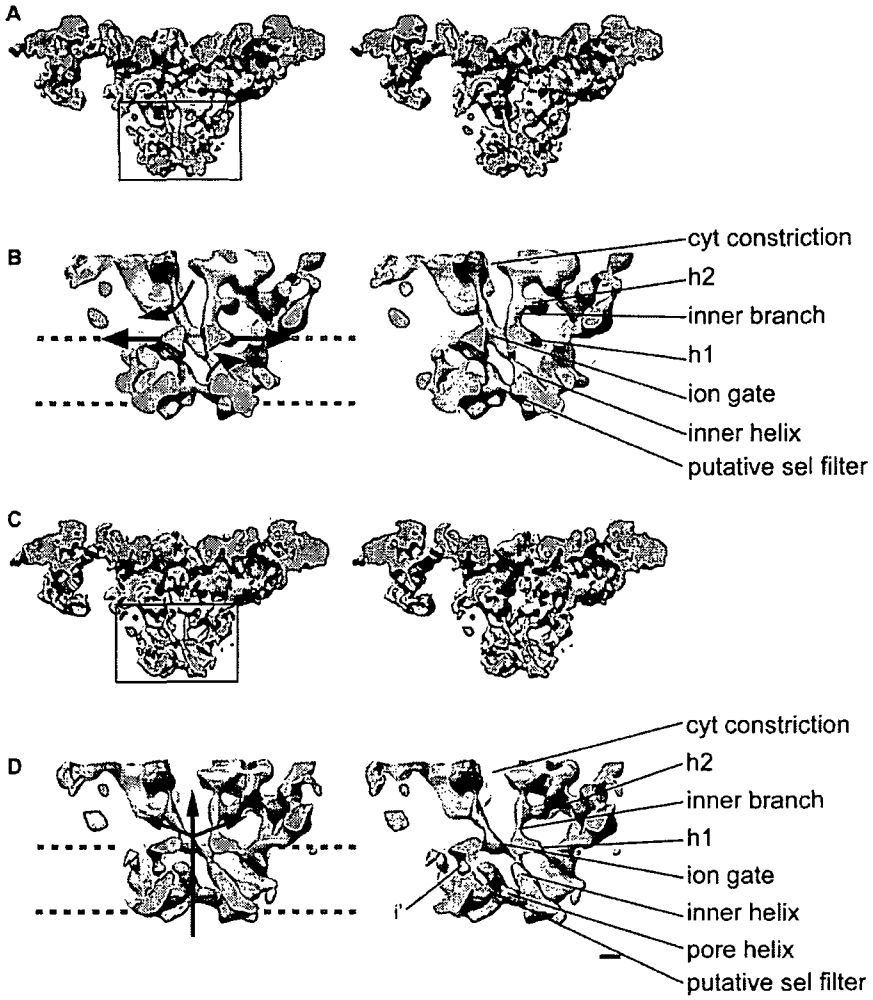

Figure 3. Stereo View of RyR1 in the Closed and Open States

(A and C) Side view of RyR1 in the closed and open states, respectively, sliced through the 4-fold axis, along a plane that is 11° from the diagonal, with the region indicated with a square magnified in (B and D). The cutting plane is in gray. The density maps are displayed at a higher threshold to reveal the inner helices and the inner branches. Note the less crowded area between the inner branches.

(B and D) The structure surrounding the ion pathway in the closed and open conformations, respectively. The region enclosed in the square in (A and C) has been magnified, and a thin slice has been cut from the back using another cutting plane parallel to the front one for better visualization of the ion pathway. The two bundles formed by the inner branches and the inner helices define the ion gate at their meeting point. Because the bundles are cut through the middle and they move upon gating, in the closed state, two inner helices are seen, whereas in the open state, one helix is seen fully and two others are partially sliced. Two inner branches are seen fully both in the open and closed states. The arrows in (B) indicate how the different structures move upon opening. Upon channel opening, the inner helices bend outwards, presumably on a Gly hinge in the peptide sequence of the presumed inner helix, the inner branches move apart, and the horizontal structures h1 move outwards. Their combined effect results in dramatic changes along the ion pathway and produce a potential novel mechanism for Ca^{2+} channel gating. In (D), the arrows indicate the pathway of the ion flow.

The identifiable features are indicated, and the abbreviations are as follows: cytosolic constriction (cyt constriction), horizontal rod-like structures (h1, h2), possible continuation of the inner helices (i'), and putative selectivity filter (putative sel filter). The gray dashed lines indicate the approximate boundary of the SR membrane. Scale bar indicates 10 Å.

doi:10.1371/journal.pbio.1000085.g003

selectivity filter surround the central cavity (see Figures 3, 8B-c, and 8D-c).

In agreement with our previous 3D structure of RyR1 [7], the transmembrane assembly of both new 3D reconstructions reveals at least six distinct regions of high density per subunit that can be attributed to α helices (Figure 8). These rod-like structures have a density >3 σ above the mean and are clearly differentiated from their surroundings; they are identified as red contoured regions in Figure 8. There is a remarkable similarity between the arrangement of all six α helices of the mammalian voltage-dependent shaker channel Kv1.2 in the open state and the putative RyR1 transmembrane α helices in the same condition (see Results and Figure 9). For the purpose of comparison, we designate the putative α helices of RyR1 as R1–R6, where R6 is the inner helix. These are named according to the comparably positioned α helices of the K^+ channel (S1–S6).

Ion Gate Opening Mechanism: Dissecting the Ion Pathway

Movement of the inner helices away from the 4-fold axis. In the closed state, the inner helices form a right-handed helical bundle constricting towards the cytoplasm (Figure 3). The

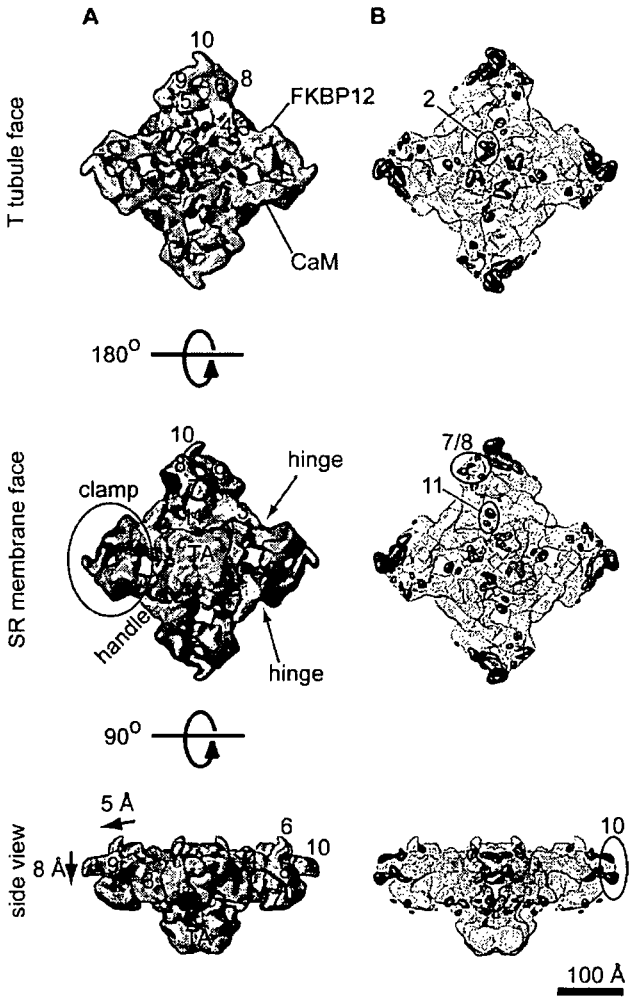

Figure 4. Domain Translocation upon Opening

(A) The superimposition of RyR1's isosurfaces in the open (magenta) and closed (green) states reveals a generalized conformational change. Upon opening the clamp, domains (especially the distal domains 7, 8, and 10) move toward the SR, domain 2 moves upwards (towards the T-tubule) and outwards, domain 11 moves outwards, and the transmembrane assembly rotates clockwise with respect to the cytoplasmic domain. The orientation of each view is indicated on the left, and the relevant features are circled. TA, transmembrane assembly.

(B) The two difference maps corresponding to the extra mass in the open (red) and closed (blue) states are superimposed on the 3D reconstruction of RyR1 in the closed state (green mesh). The "pairs" of neighboring differences correlate with the main changes observed in (A). The volumes have been filtered to a resolution of 18 Å for better visualization of the main conformational changes. The approximate binding sites of Ca^{2+}-CaM and FKBP12 are indicated. IpTxa binds at a position overlapping the Ca^{2+}-CaM binding site.

doi:10.1371/journal.pbio.1000085.g004

length of the inner helices is approximately 40 Å (from lumen to ion gate). A slight decrease in density in the region closest to the cytoplasmic side of the membrane indicates a point of flexibility. In the open conformation, the bottom halves of the inner helices (proximal to the lumen) are reoriented in four ways with respect to the closed state. They are shifted 3 Å along the 4-fold axis towards the cytosol, they are in a more vertical position with respect to the 4-fold axis—39° versus 44°—causing the portion facing the ion gate to move farther away from each other, and they are slightly bent outwards (Figure 3D). After this bend, the electron density of the inner helices becomes very weak. The inner helices clearly point to a ring of density that has a larger diameter and is less thick in the open state than in the closed state (Figures 3B, 3D, and 7B). These data confirm our previous assumption that this ring of density is the ion gate. Both the change in angle and the outwards bending appear to be directly related to a relaxation of the helical bundle and the wider ion gate. The length of the inner helices in open conformation is approximately 20 Å (from lumen until the density discontinuity). There are two equally likely possibilities for the pathway of the inner helix beyond the region of discontinuity: (1) the inner helix of RyR1 directly connects with the ion gate at the base of the adjacent inner branch, or (2) the inner helix connects with the ion gate via a short rod-like density connected to the ion gate that appears in the open state indicated by i′ in Figure 3D. Because of its more contorted trajectory, the second possibility may require an additional hinge, which would be a viable possibility based on our putative sequence assignment of the inner helix presented below.

To assess the similarity between the conformation of the inner helices of RyR1 and K^+ channel families, we compared this region of the channel to K^+ channels by docking the inner helices of K^+ channels into the cryoEM density map, followed by computation of the cross-correlation values between the two maps filtered at 10 Å resolution. We considered all the currently deposited atomic structures for the K^+ channels that include K^+ channels crystallized in the closed (KcsA and KirBac1.1) and the open (Kv1.2, KvAP, and MthK) states [15,16,27,33,34]. Pairwise comparisons indicate that the inner helices of closed-state RyR1 cross-correlate better with all closed K^+ channels than with any of the open K^+ channels (Figure 6A, filled symbols). The opposite is true for the inner helices of the open-state RyR1 (Figure 6A, open symbols). The best matches are with the closed KcsA and open KvAP for the closed and open RyR1s, respectively; see stereo pairs for each 3D reconstruction with the docked K^+ channels (Figure 6B and 6C). In the docking, the region of density discontinuity observed in the open cryoEM maps directly superimposes with the Gly (or the equivalent Pro-X-Pro) hinge of the K^+ channels [28,29,35] (arrow in Figure 6C), supporting the hypothesis that this is the site of the putative Gly hinge of RyR1 [36].

On the basis of hydropathy profiles, early studies suggested that amino acids (AA) from 4914 to 4937 make up the last transmembrane domain of RyR1 [37], and it has also been proposed that the last transmembrane domain corresponds to the inner helix of the channel [38,39]. This putative transmembrane domain has only a single Gly residue near its C-terminus, 4934. However, the position of this residue is too close to the end of the helix to act as an effective hinge. For a hinge to change the diameter of the ion gate effectively, it would need to be located in a more central location. Exclusively on the basis of structural data, others have proposed that instead, AA 4918–4948 [17] defines the last transmembrane domain. We favor this assignation. The reason for this preference is based on the fact that unlike the hydropathy profiles, α helix prediction algorithms indicate a low α helical propensity for sequence 4911–4919, and high α helical propensity for residues 4920–4952 (Figure 10). Furthermore, in the latter inner helix assignments, Gly

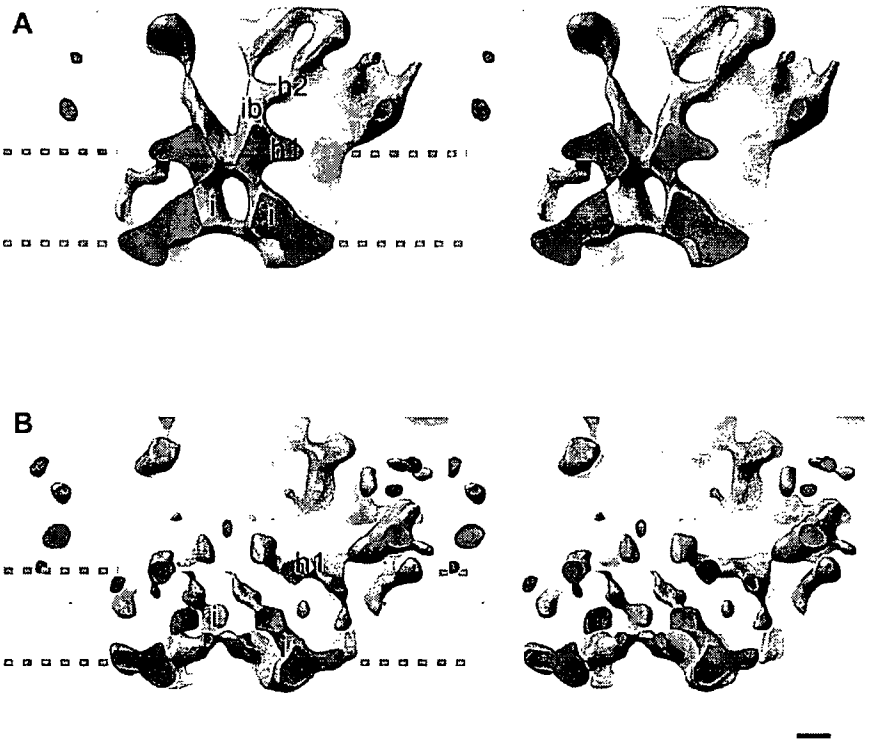

Figure 5. Previously Determined Closed RyR1 Ion Pathways

(A) RyR1 in the closed state by Samso et al., 2005 [7] (EMDB code 5014).
(B) RyR1 in the closed state by Ludtke et al., 2005 [17] (EMDB code 1275).
The orientation and representation of both 3D reconstructions is equivalent to that of the RyR1-FKBP12 3D reconstructions in the open and closed states shown in Figure 3. The thresholds of the two compared structures have been adjusted for optimal comparison. The identifiable features are indicated as follows: inner helices (i), inner branches (ib), and horizontal rod-like structures (h1). The gray dashed lines indicate the approximate boundary of the SR membrane. Scale bar indicates 10 Å.
doi:10.1371/journal.pbio.1000085.g005

4934 is in a more central position, and a second Gly residue, AA 4941, could add a second point of flexibility within the inner helix. This assignment would also place Phe 4940 in a position where it could act as a putative pore-blocking residue in the closed state [16,40]. In addition, Asp 4938 and 4945, two negative residues known to modulate RyR1 ion fluxes [41], would be located after the Gly 4934 hinge and thus be in the cytosolic vestibule, affording them the opportunity to efficiently perform such a function. Last, the longer proposed sequence (residues 4920–4952) agrees better with the 40 Å length that we measure for the complete inner helix.

Movement of the inner branches away from the 4-fold axis. In our previous closed-state 3D reconstruction, we identified four rod-like structures situated near the 4-fold axis of the structure on the cytoplasmic side of the presumed ion gate, that we named inner branches [7]. The distinct section of the inner branches in our two new 3D reconstructions, with densities >3 σ above the mean value, is approximately 21 Å long with an elongated lateral extension in the middle (h2) (Figures 3, 8B-a, and 8D-a). Both the inner branches and their lateral extension then merge with other internal cytoplasmic domains.

In the closed state, the inner branches merge with each other and form the high-density ring defining the ion gate. In the transition from the closed to the open states, the four inner branches assume a more tilted position (from ~21° to 29° with respect to the 4-fold axis), rotate 5° counterclockwise (as seen from the cytoplasmic distal domains), and move approximately 6 Å further away from each other at their midpoint. The separation of the inner branches on the cytoplasmic side of the SR membrane is directly related to the diameter of the ion gate (Figures 3, 7A, 7B, 8B-a, and 8D-a). Unlike their position in the closed state, in the open state, the inner branches do not merge, but are still attached to the wider ring (Figures 3, 7A, and 7B). Thus, it appears that by changing their position during the transition from closed to open, the inner branches participate directly in the change of the diameter of the ion gate. By directly linking the peripheral cytoplasmic domains (where many RyR1 effectors interact) to the ion gate, the inner branches appear to be strategically built to mediate long-range conformational changes, as we suggested previously based on the closed-state structure alone.

The inner branches become bulkier approximately 25 Å away from the ion gate, and in the closed conformation, they contact each other forming a 10 Å–diameter ring (the cytosolic constriction) (Figures 3 and 7A). The cytosolic constriction does not appear to have a direct role in gating since the cavity between the four branches is continuous with the cytosol through long openings similar to the side portals identified in the nAChR [42]. In the latter case, the side portals are thought to perform an electrostatic prescreen of ions. In RyR1, in which this structure is situated after the putative ion gate, we do not expect such a functional role.

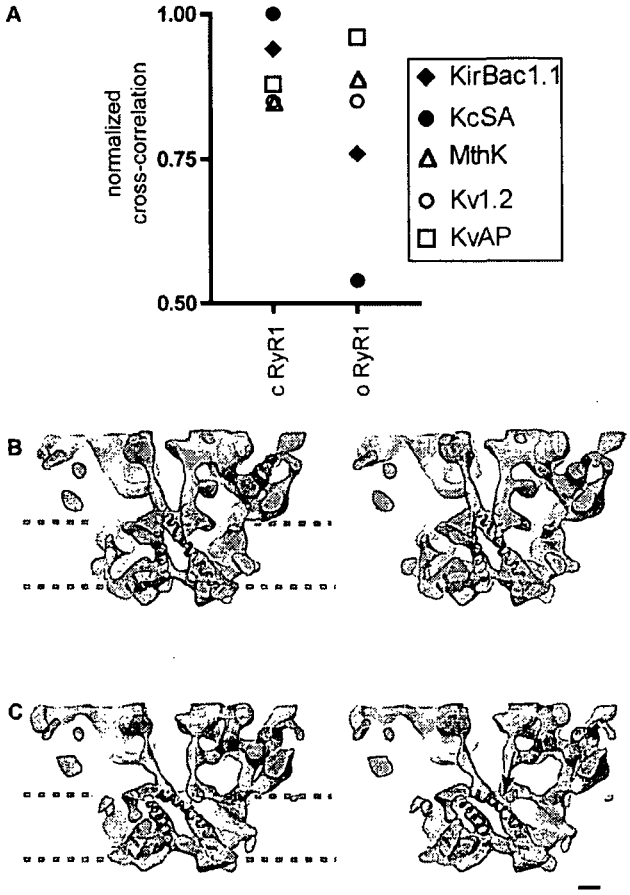

Figure 6. RyR1 Inner Helices in the Context of the Inner Helices of K^+ Channels

(A) Cross-correlation between the inner helices of five K^- channels and these of RyR1 measured for both the closed and the open RyR1. The filled symbols are indicative of K^+ channels in the closed conformation, and the open symbols are indicative of those in the open conformation. Closed K^+ channels cross-correlate better than open K^+ channels with the closed RyR1, and the situation is reversed for the open state.
(B) Stereo pair showing the docking of the inner helices of closed RyR1 with these of closed KcsA. The gray dashed lines indicate the approximate boundary of the SR membrane.
(C) Stereo pair showing the docking of the inner helices of open RyR with these of open KvAP. The arrow points to the density discontinuity in the inner helices of RyR1 that overlaps with the Gly hinge in the docked K^+ channel. Scale bar indicates 10 Å.
doi:10.1371/journal.pbio.1000085.g006

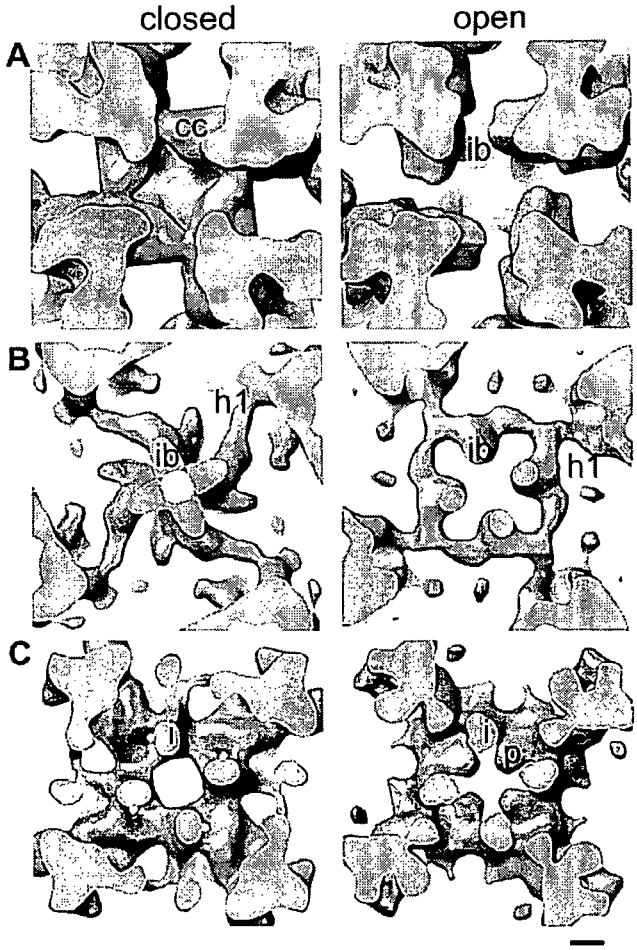

Figure 7. Isosurface Representations Showing the Main Constrictions along the Ion Pathway in the Closed and Open States

(A) The cytosolic constriction relaxes and the inner branches become more separated in the open state.
(B) The ion gate increases in diameter upon opening.
(C) The pore helices are identifiable in the open state.
The identifiable features are indicated as follows: cytosolic constriction (cc), inner helices (i), inner branches (ib), pore helices (p), and horizontal rod-like structure (h1). The region between the ion gate and the cytosolic constriction is continuous with the cytoplasm through the fenestrations situated between the inner branches. The cutting surface plane is gray in all panels, and the structures are viewed from the cytosolic side. The isosurface level for panels (B and C) is equivalent to that in Figure 3. The isosurface level for (A) has been lowered in order to display the cytosolic constriction. Note that while the ion gate and the cytosolic constriction are wider in the open state, the selectivity filter appears narrower. Scale bar indicates 10 Å.
doi:10.1371/journal.pbio.1000085.g007

However, it is conceivable that the cytosolic constriction has a role in stabilizing the closed conformation.

The sequence identity of the inner branches is not known. Since they are a density continuous with that of the ion gate, one possibility is that they are formed by part of the 4938-5037 C-terminal sequence downstream of the inner helices. We base this on the following reasoning. First, this sequence is predicted to contain critical residues involved in multimerization [43], thus a position near the 4-fold axis is a likely location because the ion gate, and/or the cytosolic constriction 25 Å away from the ion gate, would be a good candidate(s) as a multimerization site(s). Second, one of the predicted α helical segments of this region (Figure 10) has an estimated length of 21 residues, which is compatible with its physical measurements of 25 Å. Third, based on electron paramagnetic resonance (EPR) studies of the full-length KcsA channel, the sequence downstream of the inner helices was proposed to be formed by a mixture of α helix and random coil with a combined length of approximately 40 Å and a structural arrangement very similar to that found in our studies, whereby the four elongated structures run approximately parallel to the channel's 4-fold axis extending towards the cytoplasm [44]. This region has not been resolved in any of the K^+ channel atomic models determined by crystallography that we have checked [15,16,27–29]. However, the complete structure of the inner branches must be more complicated than a simple combination of α helix and

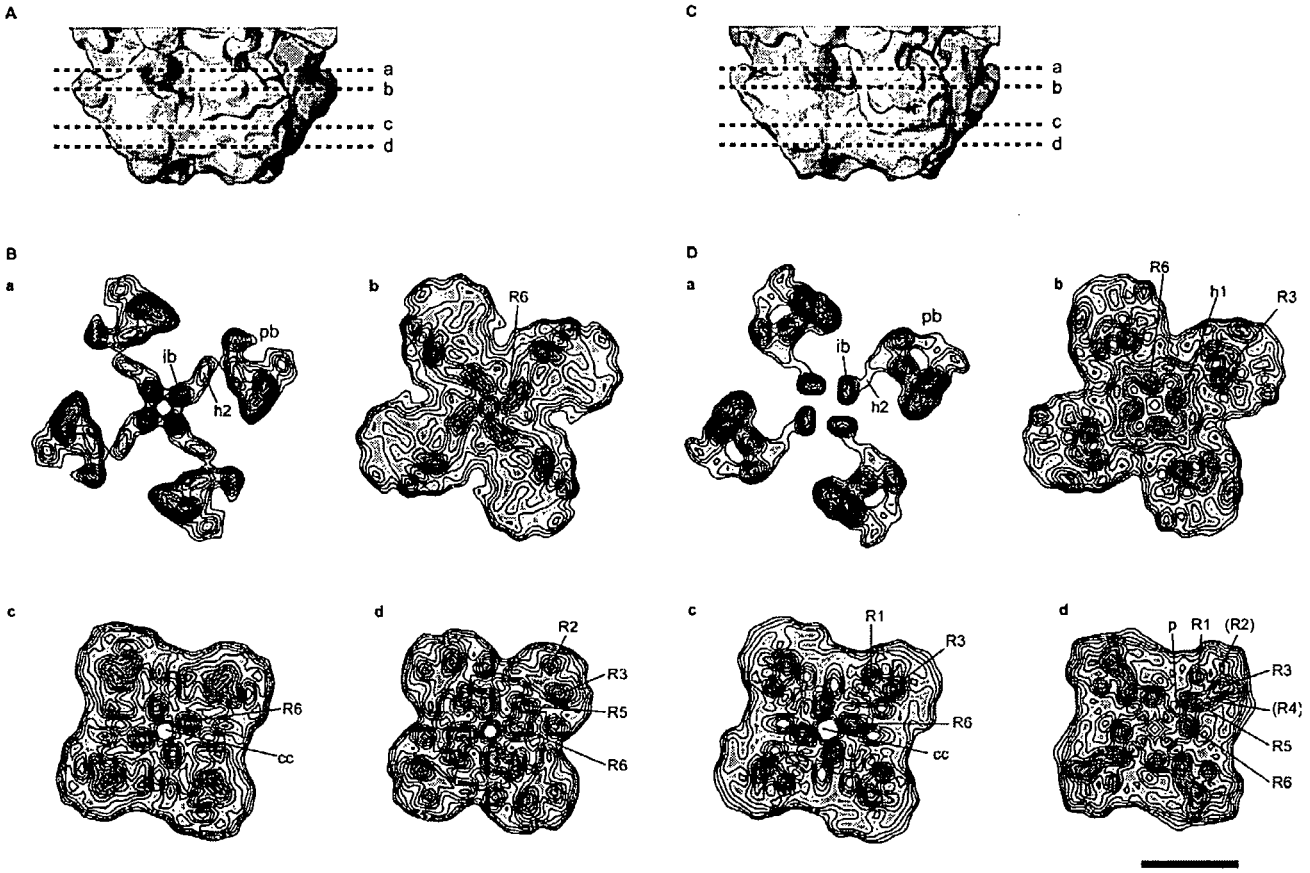

Figure 8. Slices through the Transmembrane Domain of RyR1.

(A) Side view of the transmembrane domain of RyR1 in the closed state with the positions of the slices indicated with dashed lines.
(B) Slices of the RyR1 in the closed state perpendicular to the 4-fold axis as seen from the cytoplasmic domain. The blue and red colors indicate a density of at least 2.35 σ and 3.06 σ above the mean, respectively. The contour intervals correspond to 0.176 σ increments. The higher gradient of density surrounding the perimeter of the transmembrane domain indicates the boundary of the structure. The numerals preceded by the letter R indicate putative RyR1 α helices that correspond to the six transmembrane α helices of Kv1.2 (see Figure 9); R6 corresponds to what we have previously defined as the inner helices. The numerals in parentheses indicate less defined densities that correspond in position to α helices in Kv1.2. The abbreviations are as follows: cc, central cavity; h, horizontal densities; ib, inner branches; ih, inner helices; p, pore helices; and pb, peripheral branches.
(C) Side view of the transmembrane domain of RyR1 in the open state with the positions of the slices indicated with dashed lines.
(D) Slices of the RyR1 in the open state perpendicular to the 4-fold axis as seen from the cytoplasmic domain and displayed as in (B).
Scale bar indicates 50 Å.
doi:10.1371/journal.pbio.1000085.g008

random coil since the rod-like density h2 emerges from each inner branch at a 90° angle and merges with the cytoplasmic domains (Figures 3, 8B-a, and 8D-a).

Outward movement of a planar network surrounding the ion gate. Four additional structures parallel to the cytosolic side of the SR membrane connect the ring forming the putative ion gate to the peripheral region of the transmembrane domain (h1, see Figures 3 and 7B). In the closed state in which the ion gate is smaller, the four rod-like h1 structures give the appearance of a cross. A similar structure in the K^+ channel, the slide helix, is also proposed to have an active role in gating [7,17]. The h1 densities appear to move outwards in going from the closed to the open state, also contributing to the increased diameter of the ion gate in the open state. The outward movement of the h1 densities is concomitant with the outward and upward (toward the cytoplasm) movement of the inner helices upon opening (arrows in Figure 3B), which accounts for the slightly wider and shorter appearance of the transmembrane domain in the open state.

Pore helices. Cation selectivity is performed at the selectivity filter, which has been shown to have a conserved sequence among several different cation channels such as K^+ channels, IP3Rs, and RyRs [40,45]. Single point mutations in the identical six-residue sequence of all RyRs (GGGIGD) can dramatically reduce the unitary conductance or even abolish it [46–48]. In all the crystallized K^+ channels, the selectivity filter forms a constriction that spans from the tips of the pore helices to the pore opening opposite to the ion gate. There the carbonyl residues coordinate the cations along their pathway. In our 3D reconstructions, a similar constriction between the central cavity and the luminal mouth constitutes the putative RyR1 selectivity filter. In the open state, the pore helices are clearly resolved. They protrude into the central cavity, providing a narrow passage between the central cavity and the SR lumen (Figures 3D and 7C). We are certain that pore helices in the presence of PCB 95 reflect the native open conformation of the permeation pathway because the PCB 95–stabilized conformation has a unitary Cs^+ current indis-

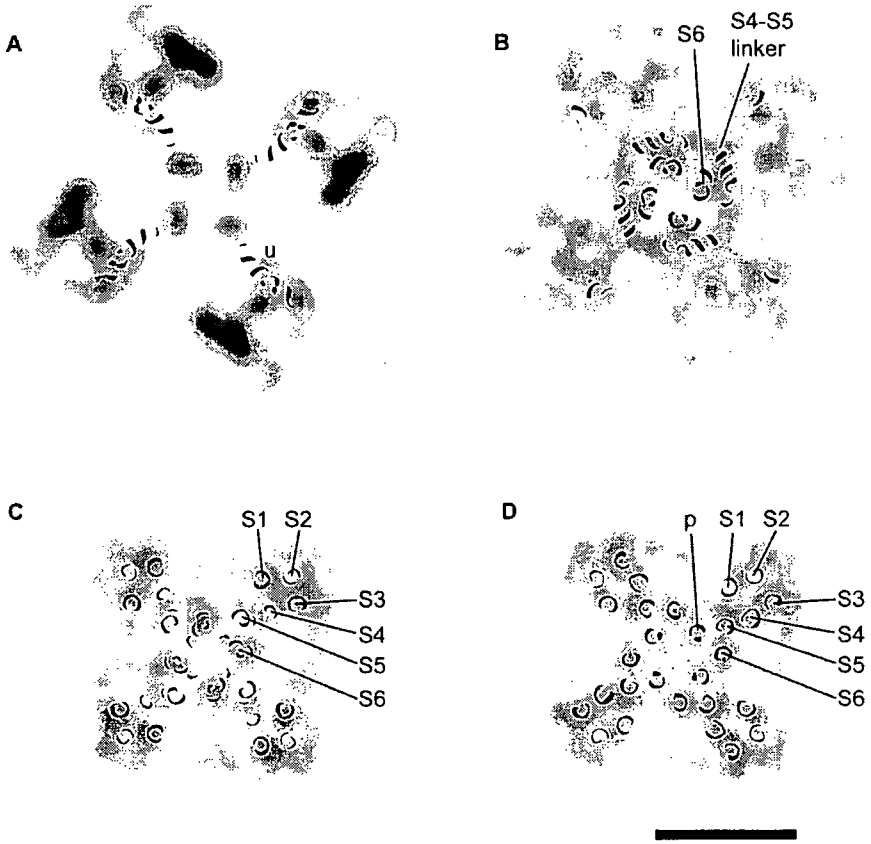

Figure 9. Slices through the Transmembrane Domain of Open RyR1 Superimposed on the Atomic Structure of Open Kv1.2

(A–D) Slices through the transmembrane domain of RyR1 in the open state perpendicular to the 4-fold axis corresponding to the positions a–d indicated in Figure 8C. The blue and red indicate a σ of at least 2.35 and 3.06 above the mean, respectively, with the slices b–d in lighter color to more clearly visualize the docked α helices of the K^+ channel. The atomic model of Kv1.2 is superimposed; only the α helical backbone is displayed. S1–S6 are transmembrane segments, p indicates the pore helix, and u an α helix within the atomic model of Kv1.2 of unknown sequence. Scale bar indicates 50 Å.
doi:10.1371/journal.pbio.1000085.g009

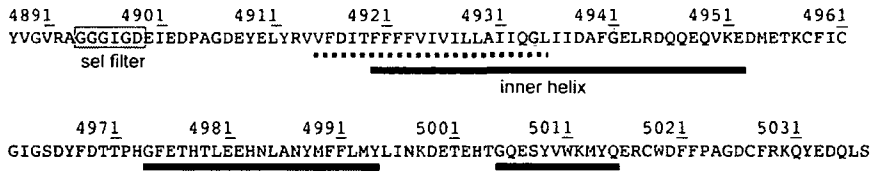

Figure 10. Secondary Structure Prediction

Predicted regions of hydropathy (dashed line) and α helix (continuous line) for the C-terminal region of RyR1. The position of the selectivity (sel) filter is also indicated. The Gly residues (highlighted in gray) are possible points of flexibility.
doi:10.1371/journal.pbio.1000085.g010

tinguishable from that measured in the presence of activating Ca^{2+} alone (Figure 1C). In the closed state, either in the absence [7] or in the presence of FKBP12, the density of the pore helices is not resolved (Figures 3B and 7C). This could be due to lack of resolution per se, or alternatively, they are closer to another density than in the open state. This can only be solved when higher resolution is attained for both states.

The change in conformation along the ion pathway during gating can be seen in Video S2.

Putting the Ion Gate Dimensions into Context

We compared the diameter of the ion gate of our open/closed RyR1-FKBP12 with that of previous 3D determinations of RyR1 in the closed state [7,17]. Furthermore, taking into account that the diameter of the K^+ and Ca^{2+} ions is very similar, around 4 Å, we compared the diameter of the ion gate of RyR1 with that of the K^+ channels and nAChR in open/closed conformations that have been determined at atomic resolution. To accomplish this for RyR1, we measured the diameter of the ion gate at a density threshold corresponding to the secondary structure (Figure 11). The diameter of the ion gate of our closed RyR1-FKBP12 and closed RyR1 [7] 3D reconstructions is 8 Å, whereas the diameter of the ion gate of the closed RyR1 obtained at similar resolution in the same conditions by another group is 15 Å [17]. The diameter we find here for the RyR1-FKBP12

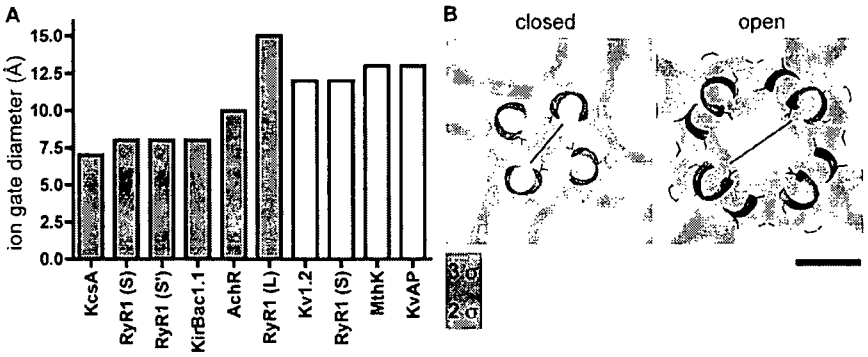

Figure 11. Ion Gate Diameters of K^+ and RyR1 Channels

(A) Comparative chart of ion gate diameters. The filled and open bars indicate closed and open channels, respectively. Three diameters are reported for closed RyR1: (S) from the current RyR1-FKBP12 reconstruction, (S') from our previous RyR1 reconstruction [7], and (L) from a previous RyR1 reconstruction done by another group [17].

(B) Section across the ion gate of RyR1 in open and closed states with the docked K^+ channels in the corresponding conformations. The black lines measure the distance between the inner edges of the inner helices of the K^+ channels and the corresponding densities within RyR1. Scale bar indicates 10 Å.

doi:10.1371/journal.pbio.1000085.g011

ion gate in the open state is 12 Å. From the known atomic structures of K^+ channels and nAChR, we took the equivalent measurement, defined by the inner edge of the inner helices, and find that in the closed state, their ion gate diameters range between 7–8 Å (closed K^+ channels, which are tetramers) and 10 Å (closed nAChR, which is a pentamer). For all of the open channels, the diameter is 12–13 Å [29,33–35].

Taken into this general context, our measurement of 8 Å for RyR1's closed ion gate falls within the values found for the closed conformations, and the measurement of 12 Å for RyR1's open ion gate corresponds to that found for the open conformations of the known K^+ channels (Figure 11). When the side chains of the K^+ channel's atomic model are taken into consideration, the actual diameter of the closed pore is 4 Å [15]. Thus, it is likely that when atomic resolution of RyR1's structure is obtained, our 8 Å diameter will result in similar pore dimensions, which is an appropriate conformation for a closed Ca^{2+} channel. Likewise, the observed increase to 12 Å diameter in the open state should be sufficient to enable Ca^{2+} flow.

Similarity of the Architecture of the Transmembrane Domains of RyR1 and Kv1.2

When the atomic structure of open Kv1.2 [35] is superimposed on the open RyR1 density map, the positions of the α helices of Kv1.2, S1–S6, correlate well with high-density regions of RyR1 (Figure 9). Starting from the 4-fold axis, we assign S6, the four inner α helices of the K^+ channel, to the four central rod-like structures (inner helices) in RyR1 (R6, see Figures 8D-b through 8D-d and 9B–9D). The tips of the pore helices in Kv1.2 also overlay those of RyR1 (p in Figures 8D-d and 9D). Four rod-like structures that are in the same position as the outer helices of the K^+ channel (S5) can be identified in the region of RyR1's transmembrane domain proximal to the lumen (R5) (see Figures 8B-d, 8D-d, and 9D). We suggest that they are the putative outer helices, or R5. The S1–S4 helices form the voltage sensor of Kv1.2. Although RyR1 does not have known voltage-sensing activity, we observe that S1–S4, which form the voltage sensor in Kv1.2, overlap with the corners of the transmembrane assembly of RyR1. Two densities in RyR1, R1 and R3, are in a similar configuration to S1 and S3, although slightly farther away from the 4-fold axis (Figures 8D-c, 8D-d, 9B, and 9D). R2, a weaker density, matches with S2, and the intervening density between R3 and R5, indicated as R4 in Figure 8D-d, could correspond to S4. At the level of the ion gate, R6 continues to overlap with S6, and the horizontal rod-like density 1 (h1) of RyR1 overlaps with the S4–S5 linker structure (Figures 7B, 8D-b, and 9B). The h2 structure coincides with an α helical structure of unknown sequence in the Kv1.2 atomic model [35] (see u in Figure 9A superimposed on the open RyR1 density map). Despite the structural similarity, we could not find sequence homology between the transmembrane segments of Kv1.2 and the aliphatic segments of RyR1. In contrast with Kv1.2, two other atomic models of K^+ channels with six transmembrane α helices per subunit [29,34] do not match well with our cryoEM density map. The region of discordance in these atomic models is the S1–S4 formation; however, this could well be the result of the presence of the Fab/Fv fragments against the voltage sensors that were needed for crystallization.

Discussion

Comparison with Previous Open-State 3D Reconstructions of RyR1

A previous 30 Å resolution reconstruction of RyR1 was prepared in conditions designed to represent the open conformation (100 μM Ca^{2+}, 100 nM ryanodine) [11]. This reconstruction indicated that in going from the closed to the open state, the protein undergoes several conformational changes: a counterclockwise rotation of the transmembrane domain with respect to the cytoplasmic assembly, an elongation of approximately 10 Å of the overall structure in the 4-fold axis direction, an opening of the clamp domains between domains 9 and 10, and an increase in pore diameter from 0 to approximately 18 Å. Two other 3D reconstructions of RyR1 at similar resolution were prepared to represent fully and transiently open states (100 μM Ca^{2+}, and 100 μM Ca^{2+}

plus 1 mM AMP-PCP, respectively) [12] also indicated an opening of the clamp domains between domains 9 and 10. In these cases, no elongation along the 4-fold axis was observed. Due to the limited resolution, the pore diameter was highly threshold-dependent and in a range between 0–7 Å diameter.

Many of these features are not compatible with our observations, and because of the low resolution of these reconstructions, some genuine structural differences were likely to have been confounded by effects resulting from low or anisotropic resolution. In our current reconstructions and a previous closed-state reconstruction [7] of RyR1, all at around 10 Å resolution, the only connection from domain 10 to the rest of the structure is domain 9, making it impossible for the clamp domains to "open" during gating by separating domains 10 and 9 [11,12]. Their observed gap is likely to be a consequence of the lower resolution and the threshold nonequivalence between the open state and closed states as it is known that the choice of threshold in low-resolution reconstructions dramatically affects the surface representations. Second, the elongation in the z direction that they observed, but was not observed in our reconstruction, is likely due to averaging of the central domains moving away from the transmembrane assembly and the peripheral domains moving toward it. In addition, the missing-cone artifact [25], whereby a large proportion of 4-fold views with respect to side views, could provoke an artifactual elongation along the 4-fold axis. Last, the diversity of dimensions for the open pore and the much lower resolution in the previous open-state 3D reconstructions [11,12] do not warrant a comparison of pore dimensions.

Control of the Ion Gate from Remote Cytoplasmic Domains

In trying to elucidate the molecular mechanism for ion gating using cryoEM, we have found that upon channel opening, structural changes in the cytoplasmic domains are coordinated with structural changes in the ion gate. All domains appear to move in an orchestrated manner, resulting in a significant lowering of density along the 4-fold axis of the protein and an increase of the ion gate diameter. The most obvious connection that we can see between changes at the cytoplasmic domains and ion gate opening is how the upward and outwards movement of the cytoplasmic domains pulls the inner branches in that same direction. Because the inner branches are directly connected to the ion gate, it is straightforward to see how their being pulled apart increases the diameter of the ion gate.

RyR1's large cytoplasmic domain interacts with several proteins such as the voltage sensor (DHPR), FKBP12, CaM, and IpTxa, and all four affect RyR1's gating. In intact skeletal muscle, RyR1 appears to open exclusively under the control of the DHPR. Removal of FKBP12 or addition of IpTxa is known to induce subconductance states, whereas CaM modulates the Ca^{2+} dependence of RyR1's probability to open. The binding sites for FKBP12, CaM, and IpTxa have been mapped by cryoEM and 3D difference mapping [8–10,49,50], and in all cases, they bind at least 130 Å away from the ion gate (positions of FKBP12 and Ca^{2+}-CaM binding sites are indicated in Figure 4A). We suggest that the conformational changes associated with gating that we have found here are very likely to be the same as the long-range allosteric pathways that convert remote signals sensed through protein/peptide/small molecule–protein interaction in RyR1's cytoplasmic domains into the appropriate response (e.g., the probability of RyR1's ion gate to open).

By superimposing the open/closed 3D reconstructions, one can observe regions of density displacement near regions that remain almost stationary. This indicates the presence of structural hinges, i.e., boundaries between regions of RyR1 that move with different breadths. The two more noticeable regions where this takes place are the crevice near domain 4, and the one between domains 5, 9, and 3 (Figure 4A). Interestingly, these hinges correspond to previously mapped binding sites. The crevice near domain 4 is the target for IpTxa and Ca^{2+}-CaM [10,50]. Likewise, the intersection between domains 5, 9, and 3, constitutes the FKBP12 binding site [9,10]. Thus, it appears that the hinges may constitute regulatory sites where binding of a relative small effector could produce optimal effect.

Solving the Controversy of the RyR1 Ion Pathway in the Closed State

It has been previously reported that the dimension of the closed ion gate in a 9.6 Å reconstruction of RyR1 is 15 Å [17]. This is surprising because it is almost twice the size of the pore we have found in our 10.2 and 10.3 Å resolution reconstructions of RyR1 in the closed state and 20% larger than the open ion gate reported here (Figure 11). A pore of 15 Å would leave a large gap that, based on the dimensions of open ion gates for other known cation channels, should not be impermeable to Ca^{2+} ions. The inner branches were not observed in this 9.6 Å 3D reconstruction, and the density in several portions of their putative inner helices is discontinuous (Figure 5B), which raises the possibility that this reconstruction was obtained from a preparation that contained a mixture of open and closed conformations. Such heterogeneity would give a low signal-to-noise ratio in those parts of the structure that change conformation during ion gating. The presence of a low signal-to-noise ratio in their reconstruction required the assistance of helix hunter [51] to identify the putative helices rather than being able to see them directly by increasing the threshold as was done here. There are several portions of their putative inner helices that do not overlap with either our closed- or open-state 3D maps (compare Figure 5B with Figures 3B, 3D, and 5A). Ludtke et al. interpreted their results as meaning that the inner helices of RyR1 in the closed state are more similar to an open than a closed K^+ channel conformation. This contradicts our report here in which cross-correlation measurements between our open and closed states and all K^+ channels indicated a direct equivalence of physiological state and inner helix conformation (Figure 6). Finally, the fact that we provide three independent 3D reconstructions supports further the ion gate dimensions and inner helix conformation of open/closed RyR1, and that they are in a similar range of these reported for the K^+ channels.

A Heuristic Gating Mechanism for RyR1

Based on our results, we propose that three structures, the inner branches, the inner helices, and h1 densities, by forming a mobile axial structure, are the three main gating effectors. In the closed state, the two right-handed bundles (inner helices, inner branches) form the high-density constriction (ion gate) at their meeting point. In going from the

closed to the open state, both sets of bundles relax and appear to contribute equally to lowering the density of the ion gate (see arrows in Figure 3B). The h1 densities also contribute to the constricting effect in the closed state and move outwards as the gate opens. The resulting profile of the pore along the ion pathway looks dramatically different as it transitions from the closed to the open state. Such a three-way mechanism appears to constitute a very efficient mechanism to open and close the ion gate and is compatible with the complex regulation of RyR1 through its interaction with the DHPR and other exogenous or intracellular modulators [52].

Concluding Remarks

In summary, we have obtained the 3D reconstructions of the hydrated RyR1-FKBP12 complex both in open and closed conformations. The use of neuroactive PCB 95 [18,53] to favor the stability of the full open conformation of the RyR1 channel enabled 3D reconstructions of the ion pathway with high detail. The conformational change of the peripheral cytoplasmic domains is directly related to conformational changes in the transmembrane domain. The architecture of the RyR1 appears to be designed to support precise long-range allosteric pathways such as these involved in efficient coupling with the voltage sensor and in the modulation by ligands such as FKBP12 and CaM. Finally, we have shown that there is a striking similarity between the architectural organization of the transmembrane α helices of the K^+ channel family and those of RyR1. Beyond this similarity, we find that the inner branches, a structure that connects the cytoplasmic domains of RyR1 to the ion gate, appear to play a direct role in ion gating.

Materials and Methods

Materials. [^{3}H]Ryanodine ([^{3}H]Ry; 60–90 Ci/mmol; >99% pure) was purchased from Perkin-Elmer New England Nuclear. PCB 95 (>99% pure) was purchased from Ultra Scientific. All other reagents were of the highest purity commercially available.

RyR1 purification. RyR1 was purified from rabbit skeletal muscle to concentrations of 2 mg/ml as previously described [7]. Prior to freezing, all RyR1s were incubated with FKBP12 (Sigma) at a molar ratio of 8× for 20–40 min. Final buffer conditions to lock the RyR1 into the closed state were 20 mM Na-MOPS (pH 7.4), 0.9 M NaCl, 0.5% CHAPS, 2 mM DTT, 2 mM EGTA, 5 μg/ml aprotinin, 5 μg/ml leupeptin, and 2.5 μg/ml Pefabloc. To set RyR1 in the open state, the same buffer was used except that 10 μM PCB 95 and 50 μM Ca^{2+} were added and EGTA was excluded.

Single-channel experiments. Bilayers were made of phosphatidylethanolamine: phosphatidylserine: phosphatidylcholine (5:3:2 w/w, Avanti Polar Lipids) dissolved in decane at a final concentration of 30 mg/ml. The bilayer partitioned two chambers (*cis* and *trans*) containing buffer solution (in mM) 500 CsCl, 50 μM Ca^{2+}, and 20 Hepes-Tris (pH 7.4) on *cis* and 50 CsCl, 7 μM Ca^{2+}, and 20 Hepes-Tris (pH 7.4) on *trans*. The addition of protein was made to the *cis* solution that was held at the virtual ground, whereas the *trans* solution was connected to the head stage input of an amplifier (Bilayer Clamp BC 525C; Warner Instruments). Purified RyR1-FKBP12 complexes preincubated for 20–40 min were introduced to *cis* solution. Upon the incorporation of a single RyR1 channel into BLM, the *cis* chamber was perfused with *cis* solution to prevent additional channel incorporation. Single-channel gating was monitored and recorded at a holding potential of −40 mV (applied to the *trans* side). The sidedness (cytosolic) of the channel was verified by the positive response to addition of micromolar Ca^{2+} and response to 2 μM ryanodine and 5 μM Ruthenium Red (at the end of the experiment). The amplified current signals, filtered at 1 kHz (Low-Pass Bessel Filter 8 Pole; Warner Instrument,) were digitized and acquired at a sampling rate of 10 kHz (Digidata 1320A; Axon-Molecular Devices). All the recordings were made for a duration between 12 s and 6 min under each experimental condition. The channel open probability (P_o) was calculated using Clampfit, pClamp software 9.0 (Axon-Molecular Devices) without further filtration.

[^{3}H]Ry binding. Equilibrium measurements of specific high-affinity [^{3}H]Ry binding were determined as previously indicated [20,54]. Junctional SR vesicles of rabbit skeletal muscle (50 μg protein/ml) were incubated with or without PCB 95 in buffer containing 20 mM HEPES (pH 7.4), 250 mM KCl, 15 mM NaCl, defined concentration of $CaCl_2$, and 2 nM [^{3}H]Ry for 3 h at 37 °C. The reactions were quenched by filtration through GF/B glass fiber filters and washed twice with ice-cold harvest buffer (20 mM Tris-HCl, or 20 mM Hepes, 250 mM KCl, 15 mM NaCl, 50 μM $CaCl_2$ [pH7.4]). Nonspecific binding was determined by incubating JSR vesicles with 1,000-fold excess unlabeled ryanodine. Each of the conditions was replicated four times in two separate junctional SR preparations, and each of the readings was performed in triplicate or quadruplicate.

Cryo-electron microscopy. A 5-μl aliquot of the 2–4 mg/ml RyR1-FKBP12 complex incubation mixture was adsorbed onto a glow-discharged quantifoil holey grid and the excess blotted off with Whatman 540 filter paper. The sample was vitrified by plunging the grid into liquid ethane. CryoEM was performed on a FEI Tecnai F20 FEG microscope operated at 200 kV. Untilted images with defoci between 2.5 and 4.0 μm were recorded on Kodak SO-163 film under standard low-dose conditions (dose <10 $e^-/Å^2$) at a nominal magnification of 50,000×.

Single-particle image processing. A total of 257 and 233 micrographs for the closed and open states, respectively, were digitized on a Zeiss SCAI scanner at a step size of 7 μm, and subsequently binned down to a final pixel size of 2.8 Å. A total of 15,625 and 18,527 particles for the closed and open states, respectively, were selected interactively using the program WEB. The defocus parameters were determined for every particle using CTFTILT [55]. Individual particles were subjected to a reference-based algorithm starting from an initial 3D model of RyR1 [7] filtered to 40 Å resolution where no substructure is detectable, thus avoiding model bias. Fifty percent of the particles from each dataset with the lowest cross-correlation with the 3D model were discarded. This was followed by several iterations of refinement until the shifts and rotations stabilized. The final number of particles was 9,331 and 8,133 particles for the closed and open states, respectively. Reference alignment and 3D reconstruction enforcing 4-fold symmetry were performed using the program FREALIGN [56], which takes account of phase and amplitude contrast transfer function (CTF) correction for every particle. This program has implemented a weighting scheme to correct for noise bias, an artifact that could result in an artificial overestimation of the resolution [57]. Resolution values were calculated according to the Fourier shell correlation (FSC) curve between two half datasets. The 0.143 cutoff [26] was chosen because it was optimistic with respect to the 5 σ noise correction calculated taking into account the 4-fold symmetry (and thus data redundancy) of the RyR1. The final 3D structure of RyR-FKBP12 was normalized and filtered to a resolution of 10.2 Å using a B factor of −300 $Å^3$. The mean and standard deviation values of the volume were calculated within a spherical mask of the same diameter as that used in the iterative alignments. For 3D difference mapping, both 3D reconstructions were filtered to 18 Å resolution and normalized by adjusting the average and standard deviation of densities in both reconstructions to the same level as previously done [9]. Then the open-state RyR1 3D reconstruction was directly subtracted from the closed-state RyR1 3D reconstruction and vice versa. No further data manipulation such as postsubtraction filtering or masking was performed. SPIDER software [58] was used for preparation of the initial volumes, normalization, 3D difference mapping, filtration of the Protein Data Bank (pdb) files for comparison with the cryoEM density maps, and calculation of cross-correlation values. Image rendering, docking of atomic structures, and alignment of the other RyR1 3D reconstruction from the database were performed in Chimera [59] (http://www.ebi.ac.uk/pdbe/emdb/). Both closed-state RyR1 3D reconstructions that have been previously published [7,17] are available in the Electron Microscopy Database (http://www.ebi.ac.uk/msd-srv/docs/emdb/).

Secondary structure prediction. Hydropathicity, transmembrane propensity, and α helical prediction analyses were performed using several packages available on public servers. The different packages for α helical prediction provided reasonable overlapping sequence segments. The proposed secondary structure is based on the PSIPRED prediction method [60] (http://bioinf.cs.ucl.ac.uk/psipred/).

Accession numbers. Electron Microscopy Data Bank (http://www.ebi.ac.uk/pdbe/emdb/) accession numbers for the structures of the RyR1 in closed and open conformations are 1606 and 1607 respectively.

Supporting Information

Video S1. Conformational Changes of RyR1 upon Gating

(1) The RyR1 alternates between its open and closed conformations while moving. (2) A vertical plane cuts through the side view until the 4-fold axis, the threshold is increased, and the transmembrane domain is magnified. (3) The RyR1 alternates between its open and closed states.

Found at doi:10.1371/journal.pbio.1000085.sv001 (1.80 MB MOV).

Video S2. Gating of RyR1 along the Ion Pathway

The viewer's perspective moves along the 4-fold axis of the RyR1, going from the cytoplasmic domains towards the SR lumen. The conformational changes are shown for the cytosolic constriction, the inner branches, the ion gate, the inner helices, and the pore helices. Found at doi:10.1371/journal.pbio.1000085.sv002 (3.58 MB MOV).

Acknowledgments

We wish to thank Dr. T. Walz for his generous sharing of the microscopy facility at the Department of Cell Biology at Harvard Medical School. We also wish to acknowledge Dr. N. Grigorieff for allowing the use of CTFTILT and FREALIGN software, Ms. X. Shen for assistance in the purification of RyR1 channels, and Ms. E. F. Cabrales and Ms. I. T. Padilla for assistance in the bilayer experiments.

Author contributions. MS collected the cryoEM data and performed image processing,and secondary structure prediction studies; WF performed the lipid bilayer and [^{3}H] binding experiments; MS, WF, INP, and PDA designed the study; MS wrote the manuscript; INP and PDA commented on and edited the manuscript.

Funding. This work was supported by American Heart Association grant AHA 0530147N and the Brigham and Women's Hospital Biomedical Research Institute Fund to Sustain Research Excellence (to MS), National Institutes of Health (NIH) ARP01-46365 and 2R01AR43140 to PDA and INP, and NIH 1 PO1 ES11269 and RO1 ES14901 to INP. The molecular electron microscopy facility at Harvard Medical School was established by a generous donation from the Giovanni Armenise Harvard Center for Structural Biology, is headed by Dr. T. Walz, and is maintained by funds from NIH-GM62580 (to T. Walz). The funders had no role in study design, data collection and analysis, decision to publish, or preparation of the manuscript.

Competing interests. The authors have declared that no competing interests exist.

References

1. Brini M, Carafoli E (2000) Calcium signalling: a historical account, recent developments and future perspectives. Cell Mol Life Sci 57: 354–370.
2. Nakai J, Dirksen RT, Nguyen HT, Pessah IN, Beam KG, et al. (1996) Enhanced dihydropyridine receptor channel activity in the presence of ryanodine receptor. Nature 380: 72–75.
3. Serysheva II, Orlova EV, Chiu W, Sherman MB, Hamilton SL, et al. (1995) Electron cryomicroscopy and angular reconstitution used to visualize the skeletal muscle calcium release channel. Nat Struct Biol 2: 18–24.
4. Radermacher M, Rao V, Grassucci R, Frank J, Timerman AP, et al. (1994) Cryo-electron microscopy and three-dimensional reconstruction of the calcium release channel/ryanodine receptor from skeletal muscle. J Cell Biol 127: 411–423.
5. Wagenknecht T, Samso M (2002) Three-dimensional reconstruction of ryanodine receptors. Front Biosci 7: d1464–1474.
6. Samso M, Wagenknecht T (1998) Contributions of electron microscopy and single-particle techniques to the determination of the ryanodine receptor three-dimensional structure. J Struct Biol 121: 172–180.
7. Samso M, Wagenknecht T, Allen PD (2005) Internal structure and visualization of transmembrane domains of the RyR1 calcium release channel by cryo-EM. Nat Struct Mol Biol 12: 539–544.
8. Samso M, Wagenknecht T (2002) Apocalmodulin and Ca2+-calmodulin bind to neighboring locations on the ryanodine receptor. J Biol Chem 277: 1349–1353.
9. Samso M, Shen X, Allen PD (2006) Structural characterization of the RyR1-FKBP12 interaction. J Mol Biol 356: 917–927.
10. Wagenknecht T, Radermacher M, Grassucci R, Berkowitz J, Xin HB, et al. (1997) Locations of calmodulin and FK506-binding protein on the three-dimensional architecture of the skeletal muscle ryanodine receptor. J Biol Chem 272: 32463–32471.
11. Orlova EV, Serysheva II, van Heel M, Hamilton SL, Chiu W (1996) Two structural configurations of the skeletal muscle calcium release channel. Nat Struct Biol 3: 547–552.
12. Serysheva II, Schatz M, van Heel M, Chiu W, Hamilton SL (1999) Structure of the skeletal muscle calcium release channel activated with Ca2+ and AMP-PCP. Biophys J 77: 1936–1944.
13. Alam A, Jiang Y (2009) High-resolution structure of the open NaK channel. Nat Struct Mol Biol 16: 30–34.
14. Miyazawa A, Fujiyoshi Y, Unwin N (2003) Structure and gating mechanism of the acetylcholine receptor pore. Nature 423: 949–955.
15. Doyle DA, Morais Cabral J, Pfuetzner RA, Kuo A, Gulbis JM, et al. (1998) The structure of the potassium channel: molecular basis of K+ conduction and selectivity. Science 280: 69–77.
16. Kuo A, Gulbis JM, Antcliff JF, Rahman T, Lowe ED, et al. (2003) Crystal structure of the potassium channel KirBac1.1 in the closed state. Science 300: 1922–1926.
17. Ludtke SJ, Serysheva II, Hamilton SL, Chiu W (2005) The pore structure of the closed RyR1 channel. Structure (Camb) 13: 1203–1211.
18. Wong PW, Brackney WR, Pessah IN (1997) Ortho-substituted polychlorinated biphenyls alter microsomal calcium transport by direct interaction with ryanodine receptors of mammalian brain. J Biol Chem 272: 15145–15153.
19. Wong PW, Pessah IN (1996) Ortho-substituted polychlorinated biphenyls alter calcium regulation by a ryanodine receptor-mediated mechanism: structural specificity toward skeletal- and cardiac-type microsomal calcium release channels. Mol Pharmacol 49: 740–751.
20. Pessah IN, Stambuk RA, Casida JE (1987) Ca2+-activated ryanodine binding: mechanisms of sensitivity and intensity modulation by Mg2+, caffeine, and adenine nucleotides. Mol Pharmacol 31: 232–238.
21. Hille B (2001) Ion channels of excitable membranes. 3rd edition. Sunderland (Massachusetts): Sinauer Associates. 814 p.
22. Wong PW, Pessah IN (1997) Noncoplanar PCB 95 alters microsomal calcium transport by an immunophilin FKBP12-dependent mechanism. Mol Pharmacol 51: 693–702.
23. Timerman AP, Ogunbumni E, Freund E, Wiederrecht G, Marks AR, et al. (1993) The calcium release channel of sarcoplasmic reticulum is modulated by FK-506-binding protein. Dissociation and reconstitution of FKBP-12 to the calcium release channel of skeletal muscle sarcoplasmic reticulum. J Biol Chem 268: 22992–22999.
24. Mayrleitner M, Timerman AP, Wiederrecht G, Fleischer S (1994) The calcium release channel of sarcoplasmic reticulum is modulated by FK-506 binding protein: effect of FKBP-12 on single channel activity of the skeletal muscle ryanodine receptor. Cell Calcium 15: 99–108.
25. Glaeser RM, Tong L, Kim SH (1989) Three-dimensional reconstructions from incomplete data: interpretability of density maps at "atomic" resolution. Ultramicroscopy 27: 307–318.
26. Rosenthal PB, Henderson R (2003) Optimal determination of particle orientation, absolute hand, and contrast loss in single-particle electron cryomicroscopy. J Mol Biol 333: 721–745.
27. Long SB, Tao X, Campbell EB, MacKinnon R (2007) Atomic structure of a voltage-dependent K+ channel in a lipid membrane-like environment. Nature 450: 376–382.
28. Jiang Y, Lee A, Chen J, Cadene M, Chait BT, et al. (2002) The open pore conformation of potassium channels. Nature 417: 523–526.
29. Jiang Y, Lee A, Chen J, Ruta V, Cadene M, et al. (2003) X-ray structure of a voltage-dependent K+ channel. Nature 423: 33–41.
30. Fujiyoshi Y (1998) The structural study of membrane proteins by electron crystallography. Adv Biophys 35: 25–80.
31. Unwin N (1993) Nicotinic acetylcholine receptor at 9 A resolution. J Mol Biol 229: 1101–1124.
32. Chiu W, Baker ML, Jiang W, Dougherty M, Schmid MF (2005) Electron cryomicroscopy of biological machines at subnanometer resolution. Structure (Camb) 13: 363–372.
33. Jiang Y, Lee A, Chen J, Cadene M, Chait BT, et al. (2002) Crystal structure and mechanism of a calcium-gated potassium channel. Nature 417: 515–522.
34. Lee SY, Lee A, Chen J, MacKinnon R (2005) Structure of the KvAP voltage-dependent K+ channel and its dependence on the lipid membrane. Proc Natl Acad Sci U S A 102: 15441–15446.
35. Long SB, Campbell EB, Mackinnon R (2005) Crystal structure of a mammalian voltage-dependent Shaker family K+ channel. Science 309: 897–903.
36. Welch W, Rheault S, West DJ, Williams AJ (2004) A model of the putative pore region of the cardiac ryanodine receptor channel. Biophys J 87: 2335–2351.
37. Zorzato F, Fujii J, Otsu K, Phillips M, Green NM, et al. (1990) Molecular cloning of cDNA encoding human and rabbit forms of the Ca2+ release channel (ryanodine receptor) of skeletal muscle sarcoplasmic reticulum. J Biol Chem 265: 2244–2256.
38. Du GG, Sandhu B, Khanna VK, Guo XH, MacLennan DH (2002) Topology of the Ca2+ release channel of skeletal muscle sarcoplasmic reticulum (RyR1). Proc Natl Acad Sci U S A 99: 16725–16730.

39. Williams AJ, West DJ, Sitsapesan R (2001) Light at the end of the Ca(2+)-release channel tunnel: structures and mechanisms involved in ion translocation in ryanodine receptor channels. Q Rev Biophys 34: 61–104.
40. Schug ZT, da Fonseca PC, Bhanumathy CD, Wagner L 2nd, Zhang X, et al. (2008) Molecular characterization of the Inositol 1,4,5-trisphosphate receptor pore-forming segment. J Biol Chem 283: 2939–2948.
41. Xu L, Wang Y, Gillespie D, Meissner G (2006) Two rings of negative charges in the cytosolic vestibule of type-1 ryanodine receptor modulate ion fluxes. Biophys J 90: 443–453.
42. Unwin N (2005) Refined structure of the nicotinic acetylcholine receptor at 4A resolution. J Mol Biol 346: 967–989.
43. Lee EH, Allen PD (2007) Homo-dimerization of RyR1 C-terminus via charged residues in random coils or in an alpha-helix. Exp Mol Med 39: 594–602.
44. Cortes DM, Cuello LG, Perozo E (2001) Molecular architecture of full-length KcsA: role of cytoplasmic domains in ion permeation and activation gating. J Gen Physiol 117: 165–180.
45. Balshaw D, Gao L, Meissner G (1999) Luminal loop of the ryanodine receptor: a pore-forming segment? Proc Natl Acad Sci U S A 96: 3345–3347.
46. Zhao M, Li P, Li X, Zhang L, Winkfein RJ, et al. (1999) Molecular identification of the ryanodine receptor pore-forming segment. J Biol Chem 274: 25971–25974.
47. Du GG, Guo X, Khanna VK, MacLennan DH (2001) Functional characterization of mutants in the predicted pore region of the rabbit cardiac muscle Ca(2+) release channel (ryanodine receptor isoform 2). J Biol Chem 276: 31760–31771.
48. Lynch PJ, Tong J, Lehane M, Mallet A, Giblin L, et al. (1999) A mutation in the transmembrane/luminal domain of the ryanodine receptor is associated with abnormal Ca2+ release channel function and severe central core disease. Proc Natl Acad Sci U S A 96: 4164–4169.
49. Wagenknecht T, Grassucci R, Berkowitz J, Wiederrecht GJ, Xin HB, et al. (1996) Cryoelectron microscopy resolves FK506-binding protein sites on the skeletal muscle ryanodine receptor. Biophys J 70: 1709–1715.
50. Samso M, Trujillo R, Gurrola GB, Valdivia HH, Wagenknecht T (1999) Three-dimensional location of the imperatoxin A binding site on the ryanodine receptor. J Cell Biol 146: 493–499.
51. Jiang W, Baker ML, Ludtke SJ, Chiu W (2001) Bridging the information gap: computational tools for intermediate resolution structure interpretation. J Mol Biol 308: 1033–1044.
52. Fill M, Copello JA (2002) Ryanodine receptor calcium release channels. Physiol Rev 82: 893–922.
53. Kenet T, Froemke RC, Schreiner CE, Pessah IN, Merzenich MM (2007) Perinatal exposure to a noncoplanar polychlorinated biphenyl alters tonotopy, receptive fields, and plasticity in rat primary auditory cortex. Proc Natl Acad Sci U S A 104: 7646–7651.
54. Pessah IN, Waterhouse AL, Casida JE (1985) The calcium-ryanodine receptor complex of skeletal and cardiac muscle. Biochem Biophys Res Commun 128: 449–456.
55. Mindell JA, Grigorieff N (2003) Accurate determination of local defocus and specimen tilt in electron microscopy. J Struct Biol 142: 334–347.
56. Grigorieff N (2007) FREALIGN: high-resolution refinement of single particle structures. J Struct Biol 157: 117–125.
57. Stewart A, Grigorieff N (2004) Noise bias in the refinement of structures derived from single particles. Ultramicroscopy 102: 67–84.
58. Frank J, Radermacher M, Penczek P, Zhu J, Li Y, et al. (1996) SPIDER and WEB: processing and visualization of images in 3D electron microscopy and related fields. J Struct Biol 116: 190–199.
59. Huang CC, Couch GS, Pettersen EF, Ferrin TE (1996) Chimera: an extensive molecular modeling application constructed using standard components. Pac Symp Biocomput 1: 724.
60. Bryson K, McGuffin LJ, Marsden RL, Ward JJ, Sodhi JS, et al. (2005) Protein structure prediction servers at University College London. Nucleic Acids Res 33: W36–38.